Title

- Axo-axonic synaptic input drives homeostatic plasticity by tuning the axon initial segment structurally and functionally
- AIS plasticity driven by chandelier cell input

Authors

Rui Zhao,[1]† Baihui Ren,[3]† Yujie Xiao,[4]† Jifeng Tian,[1] Yi Zou, [1] Jiafan Wei,[1] Yanqing Qi, [1] Ankang Hu, [5] Xiaoying Xie,[1] Z. Josh Huang,[6,7] Yousheng Shu,[4]*Miao He,[1]* Jiangteng Lu, [2,3]* Yilin Tai[1]*

Affiliations

1, Institutes of Brain Science, State Key Laboratory of Medical Neurobiology and MOE Frontiers Center for Brain Science, Department of Neurobiology, Zhongshan Hospital, Fudan University, Shanghai 200032, China.

2, Songjiang Research Institute, Shanghai Songjiang District Central Hospital, Shanghai Jiao Tong University, School of Medicine, Shanghai 200025, China.

3, Center for Brain Science of Shanghai Children's Medical Center, Department of Anatomy and Physiology, School of Medicine, Shanghai Jiao Tong University, Shanghai 200127, China.

4, Department of Neurology, Huashan Hospital, Institute for Translational Brain Research, State Key Laboratory of Medical Neurobiology, MOE Frontiers Center for Brain Science, MOE Innovative Center for New Drug Development of Immune Inflammatory Diseases, Fudan University, Shanghai 200032, China

5, Department of Neurosurgery, Huashan Hospital; Shanghai Medical College, Fudan University, Shanghai 200032, China

6, Department of Neurobiology, Duke University Medical Center, Durham, NC 27710, USA

7, Department of Biomedical Engineering, Duke University Pratt School of Engineering, Durham, NC 27708, USA

† These authors contributed equally to this work

Yilin Tai: taiyilin@fudan.edu.cn

Jiangteng Lu: jiangtenglu@shsmu.edu.cn

Miao He: hem@fudan.edu.cn

Yousheng Shu: yousheng@fudan.edu.cn

Abstract

Homeostatic plasticity maintains the stability of functional brain networks. The axon initial segment (AIS), where action potentials start, undergoes dynamic adjustment to exert powerful control over neuronal firing properties in response to network activity changes. However, it is poorly understood whether this plasticity involves direct synaptic input to the AIS. Here we show that changes of GABAergic synaptic input from chandelier cells (ChCs) drive homeostatic tuning of the AIS of principal neurons (PNs) in the prelimbic (PL) region, while those from parvalbumin-positive basket cells do not. This tuning is evident in AIS morphology, voltage-gated sodium channel expression, and PN excitability. Moreover, the impact of this homeostatic plasticity can be reflected in animal behavior. Social behavior, inversely linked to PL PN activity, shows time-dependent alterations tightly coupled to changes in AIS plasticity and PN excitability. Thus, AIS-originated homeostatic plasticity in PNs may counteract deficits elicited by imbalanced ChC presynaptic input at cellular and behavioral levels.

Teaser

Axon initial segment dynamically responds to changes in local input from chandelier cells to prevent abnormal neuronal functions.

MAIN TEXT

Introduction

The axon initial segment (AIS) is a highly specialized cellular compartment localized at the proximal axon of the neuron. It serves as a gatekeeper by filtering the somato-dendritic proteins to maintain the neuronal polarity (*1-4*). More importantly, AIS contributes to the initiation of action potential (AP) as it provides docking sites for high density of voltage-gated sodium channels, which makes AIS the most excitable part of a neuron (*5-9*). The precise position relative to the cell body, the morphology of the AIS, the voltage-gated ion channel expression at the AIS, as well as axo-axonic synaptic input to the AIS could have substantial impacts on AP generation, propagation, and temporal precision (*10-16*). Therefore, subtle changes in the AIS structure or molecular composition are capable to regulate the neuronal output.

Neurons have the ability to tune themselves to maintain the stability of the network at multiple levels (*17*). Recent studies have shown that AIS undergoes plastic changes in response to alterations in network activity (*11, 12, 18-20*). The length of the AIS and its precise location relative to the cell body dynamically adapt to global depolarization in cultured dentate granule cells (*11*). Additionally, sensory deprivation by either removing cochlea or depriving the whisker-to-barrel pathway leads to the elongation of the AIS, coupled with changes in ion channel expression and increased intrinsic excitability (*12, 19*). Conversely, increased network activity through sensory input or exposure to an enriched environment induces the shortening of the AIS and shapes the channel distribution and neuronal intrinsic excitability (*19-21*). Such homeostatic adaptations of AIS at the structural and functional levels are believed to contribute to regulation of neuronal output (*22*), counteracting pathological conditions under injury or disease, thereby maintaining the stability of dynamic network activity (*23*).

While chronic (hours to days) alteration of network activity can result in homeostatic scaling of the AIS at the postsynaptic principal neurons (PNs), another form of regulation exerts

direct impact on neuronal output from the AIS: the axo-axonic synaptic input to the AIS from the axo-axonic cells (AACs). As a unique subdomain on the axon that receives synaptic input, the AIS of neocortical PN receives synaptic inputs predominantly from a distinctive type of AACs, the ChCs (*24*). By positioning their axonal terminals (called "cartridges") on the AIS to form GABAergic axo-axonic synapses, ChCs are thought to exert powerful control over PN firing to suppress irrelevant and excessive excitatory activity in neuronal networks (*25-30*). In the basal lateral amygdala (BLA), a single AP from a single AAC is sufficient to initiate sharp wave ripples (SWRs) through the local circuit (*31*). The strong impact of ChCs on PN firing raises the question of whether local alterations of ChCs input are sufficient to drive PN homeostatic plasticity by tuning the AIS and whether it contributes to functional adaptations.

In this study, we investigated the impact of chronic alterations of axo-axonic synaptic input on the structure and function of the AIS of PNs in the prelimbic (PL) region of the medial frontal cortex (mPFC). We also explored the potential link between cellular homeostatic changes and behavioral alterations by tracking their temporal profiles. Acute manipulation of ChCs altered inhibitory input to the PL PNs without inducing plastic changes in the AIS, leading to changes in social behavior, a prominent behavior controlled by PL PNs. Chronic alterations in ChC synaptic input induced plastic structural and molecular changes in the AIS of PL PNs, and changes in PN excitability. These homeostatic changes in PL PNs counterbalanced the disturbed ChC inhibitory input. Notably, the recovery of social impairment caused by altered ChC input occurred when homeostatic plasticity took place in PL PNs. These results suggest that AIS-originated homeostatic plasticity is associated with a physiological function in maintaining balanced neuronal activity and normal animal behavior.

Results

Genetic ablation of ChCs leads to reduced synaptic input to the AIS

To assess the impact of direct synaptic input on AIS plasticity, we used an intersectional genetic strategy to label and manipulate ChCs (*32, 33*). To do this, two sets of driver lines are involved (Fig. 1A). The first driver line was the *knock-in* mouse driver line, *Unc5b-2A-Cre^{ERT2}* (referred to as *Unc5b-CreER* below)(*25*), which was created based on the fact that Unc5b expression is largely restricted to ChCs (*34*). However, crossing *Unc5b-CreER* driver line with the *Ai14* reporter line (*Rosa26-loxpSTOPloxp-tdTomato*) resulted in tdTomato expression in both ChCs and capillary endothelial cells (fig. S1). Therefore, we introduced the second driver line, the *Nkx2.1-Flp*, in which Flippase (Flp) is driven from the *Nkx2.1* promotor. The *Nkx2.1* lineage includes most of the interneurons born from medial ganglion eminence (MGE), of which the ventral area is where ChCs are born (*35, 36*). By combining the *Unc5b-CreER* and *Nkx2.1-Flp* driver lines with the dual recombinase-dependent reporter line, *Ai65*, we were able to specifically label ChCs with high efficiency (fig. S2). In the mPFC, genetically labeled neurons were particularly enriched in cortical layer 2 (L2) with the typical chandelier-like morphology. The axonal terminals innervated the AIS of the PNs, forming the "cartridges" with multiple boutons (fig. S2). No capillary endothelial cells were observed, indicating that the intersectional strategy allowed for restricted gene expression in ChCs. These results are consistent with the recent preprint study that has utilized the same intersectional strategies (*33*).

To genetically ablate ChCs, we used intersectional Tau$^{\text{loxP-STOP-loxP-FRT-STOP-FRT-DTR}}$ (*Tau-ds-DTR*) mice (*37*), in which the human diphtheria toxin receptor (DTR) gene is driven by the *Tau* promoter (Fig. 1A). DTR expression is not activated until the removal of both of the STOP cassettes by Cre and Flp DNA recombinase. Upon entry of diphtheria toxin (DT) through DTR, DT blocks protein synthesis in the target cell, leading to the eventual death of the cell. By combining the *Tau-ds-DTR line* with *Unc5b-CreER:Nkx2.1-Flp:Ai65* line, specific expression of DTR together with tdTomato in ChCs could be achieved. To determine the efficiency of genetic ablation of ChCs, *Unc5b-CreER:Nkx2.1-Flp:Tau-ds-DTR*$^{+/-}$*:Ai65* mice were given tamoxifen (TMX) at P21 and P23 to turn on the expression of DTR and tdTomato in ChCs. Two weeks after TMX induction, mice were intraperitoneally (i.p.) injected with DT (50 μg/kg) at P37 and P39 to ablate the ChCs. The efficiency of genetic ablation was analyzed one week after DT application (Fig. 1A). We found a marked reduction in ChC cell number and their innervation to the AIS (Fig. 1B and 1C). There was an 81.06% reduction in tdTomato-positive cells in the PL and infralimbic (IL) regions of the mPFC in the DTR-expressing mice compared with their littermate control (Fig. 1B and 1D). Meanwhile, compared with 76.08% of PN AISs were innervated by tdTomato-positive cartridges in layer 2/3 (L2/3) of mPFC in the control littermates, only 21.77% of the AISs were innervated in the DTR-expressing mice, suggesting that the ablation of ChCs diminished their innervation on the PN AIS (Fig. 1C and 1E). Furthermore, to assess whether the ablation of ChCs resulted in overall reduction of GABAergic synaptic input on the AIS, we analyzed the number of VGAT and gephyrin puncta at the AIS. We found that both VGAT and gephyrin puncta at the AIS were markedly reduced in the DTR-expressing mice compared to their littermates (Fig. 1F to 1I). Therefore, we established an efficient way to reduce GABAergic synapses at the AIS of PNs through the ablation of ChCs, which enabled us to explore whether and how axo-axonic GABAergic synaptic input contributes to AIS physiology.

Reduction of AIS GABAergic synapses results in homeostatic changes in AIS morphology and physiology

To characterize the impact of ChC ablation on postsynaptic PN AIS properties, we analyzed the AIS of L2 PNs in the mPFC as they are densely innervated by ChCs (fig. S2). Using immunohistochemical staining for Ankyrin-G (AnkG), the master organizer of the AIS molecular assembly and a well-established marker of the AIS for morphological analysis (*38*), we observed that the length of the AIS was significantly shortened in mPFC L2 of the DTR-expressing mice compared to their littermate controls (Fig. 2A and 2B), with no detectable changes regarding their width or the distance to cell body (fig. S3). Next, we examined the distribution of voltage-gated Na^+ (Na_v1) channels as they are the most relevant channels clustered on the AIS that contribute to action potential initiation. The endocytosis of Na_v1 at the distal AIS depolarizes the threshold for AP generation and is one of the significant outcomes during AIS plasticity in cultured hippocampal neurons (*39*). Immunostaining of Pan Na_v1 revealed that the expression level of the Na_v1 family was significantly reduced after the ablation of ChCs (Fig. 2C-2E). Among the Na_v1 family members, $Na_v1.2$ and $Na_v1.6$ are the two major members with enriched expression on the AIS of PNs(*40, 41*). With the lowest activation threshold, $Na_v1.6$ has been shown to contribute to the initiation of the AP (*5, 42*). While $Na_v1.6$ consistently exhibits enriched expression on the AIS, the enrichment of $Na_v1.2$ decreases as development progresses in the cortex (*40, 43*). Therefore, we further focused on the expression of $Na_v1.6$, which is closely associated to AP initiation, after ablating ChCs. We found that the expression of $Na_v1.6$ was significantly reduced in the DT treated mice compared to their littermate

controls (Fig. 2F and 2G). However, the distribution of $Na_v1.6$ along the AIS was not changed, remaining enriched at the distal AIS (Fig. 2H).

To examine whether the ablation of GABAergic synapses on the AIS was associated with electrophysiological changes, we performed whole-cell patch recordings in L2 PNs of the mPFC (Fig. 2I). We observed an increased in AP threshold, as illustrated by the AP phase plot (Fig. 2J and 2K), with no change in AP amplitude and half width (Fig. 2L and table S1), suggesting a decrease in neuronal excitability. While we did not detect any changes in resting membrane potential (RMP) and input resistance (R_{in}) (table S1), there was a reduction in firing frequency of mPFC L2 PNs in DT-treated mice (Fig. 2M).

Taken together, the ablation of ChCs and the resulting reduction in GABAergic synaptic input to the AIS induced the shortening of the PN AIS, a reduction in Na_v1 expression, and an increase in AP threshold. These plastic changes in AIS properties aligned with the trend of decreased neuronal excitability. Following the ablation of ChCs, that led to a reduction in inhibitory input to the AIS, a decrease in neuronal excitability of the PNs was observed, suggesting the presence of a potential homeostatic mechanism to counteract the diminished inhibition to the PNs. We next set out to further corroborate this hypothesis.

Blocking axo-axonic synaptic transmission induces homeostatic changes in PL PNs

Although genetic ablation of ChCs provided a valuable tool to study the function of axo-axonic synapse, global cell loss might trigger microglia activation and neuroinflammation, introducing undesirable artifacts (*44*). To further test our hypothesis, we locally injected an adeno-associated virus (AAV) encoding a Cre recombinase-dependent tetanus toxin (DIO-Tettox) into the PL region of the mPFC of *Unc5b-CreER* mice to specifically block synaptic transmission of L2 ChCs in a restricted brain region (Fig. 3A). As AAV9 has limited tropism toward capillary endothelial cells (*45*), we did not identify any endothelial cells infected by the AAV we used in this study. To avoid any batch effects, we stereotaxically injected DIO-Tettox-2A-mCherry virus into the PL of one hemisphere and injected DIO-tdTomato control virus contralaterally of the other hemisphere in the same animal (Fig. 3B). Then, we introduced i.p. injection of TMX two days after viral injection to induce Tettox expression. Our results revealed that the levels of VAMP2, the substrate of Tettox, which is critical for the fusion of presynaptic vesicles to the plasma membrane, in the ChC boutons began to decrease from 2 weeks post-viral induction (p.i.) at P46. This reduction continued at 3 weeks p.i. (fig. S4). Consequently, we initiated our tracking of potential changes in the AIS starting from P46. At this stage, the E_{Cl} had become hyperpolarizing (*46, 47*), and the inhibitory effect of GABA on the AIS was evident (fig. S5) (*48*).

To track the time course when chronic inhibition from blocking axo-axonic synaptic transmission exerts its impact on AIS physiology, we performed immunostaining against AnkG and $Na_v1.6$ at three time points: 2 weeks (P46), 3 weeks (P53) and 4 weeks (P60) p.i. (Fig. 3C). At 2 weeks p.i., we did not observe any detectable changes. However, starting from 3 weeks p.i., we observed alterations in the length of the AIS (Fig. 3D), while the expression level of $Na_v1.6$ showed a trend of reduction ($P = 0.105$). By 4 weeks p.i., both the shortening of the AIS and the reduction in AIS $Na_v1.6$ expression became siginificant (Fig. 3D and 3E). At this point, the expression of somatic $Na_v1.6$ was not changed (fig. S6). These structural and molecular changes in the AIS suggest a decrease in the excitability of postsynaptic PNs which may counteract the weakened inhibitory input.

To substantiate this hypothesis, we further performed whole-cell patch recording in L2 PNs at corresponding time points. At 2 weeks p.i., we did not observe any alterations in AP threshold, AP amplitude, or neuronal excitability in the PL PNs (Fig. 3F to 3H). By 3 weeks p.i., while AIS shortening had started, we did not observe substantial changes in AP threshold, AP amplitude, or firing frequency in the PL PNs (Fig. 3I to 3K). Notebly, there was a trend towards an increase in the AP threshold (P = 0.101), suggesting that slight changes were underway, although not yet sufficient to impact neuronal firing frequency. At 4 weeks p.i., the AP threshold was significantly increased in the Tettox group compared with the control group (Fig. 3L and 3M), while the AP amplitude was decreased (Fig. 3N). Moreover, the AP firing rate, induced by the injection of stepped currents, was also reduced, suggesting that the excitability of PNs was decreased when chronically blocking axo-axonic synaptic transmission (Fig. 3O). Of all the time points, the AP half width, the RMP and the R_{in} remained unchanged (table S1).

In summary, the chronic reduction of axo-axonic input leads to shortened AIS and decreased AIS $Na_v1.6$ expression. Importantly, the timing of electrophysiological changes of PNs aligns with the observed structural and molecular changes of the AIS. These findings are consistent with the phenotypes observed in genetic ablation of ChCs and provide support for the hypothesis that the loss of axo-axonic inhibition triggers homeostatic changes in PL PNs. These changes originate from the AIS and aim to reduce neuronal excitability as a compensatory mechanism in response to the loss of ChC inhibition.

Chronic activation of ChCs elicits homeostatic plasticity of the PN AIS

We next explore whether chronic activation of ChCs could induce plastic changes in the opposite direction at the AIS. We used designer receptors exclusively activated by designer drugs (DREADDs), hM3Dq, to increase the axo-axonic synaptic activity. We virally expressed Cre-dependent DIO-hM3Dq or DIO-EGFP in each of the hemispheres of the *Unc5b-CreER* mouse, respectively, followed by TMX induction 2 days later (Fig. 4A and 4B). After 2 weeks, at P46, we first verified that the CNO application increased the firing rate of ChCs expressing hM3Dq (fig. S7). Then, CNO was applied twice a day for one week to elicit chronic activation of ChC (Fig. 4A). Upon the 4th day of CNO application, we did not observe any immediate changes in AIS properties or neuronal excitability (fig. S8). However, after chronic activation of ChCs for 7 days, we observed a significant elongation of the PN AISs and an increase in Na_v 1.6 expression (Fig. 4C-4E). In parallel to this, by whole-cell patch recording, we found that the PNs exhibited a decrease in AP threshold (Fig. 4F and 4G) with a trend of increased AP amplitude (Fig. 4H and table S1). The neuronal excitability of the L2 PNs in the PL was significantly increased after 7 days of chronic activation (Fig. 4I).

Taken together, we found that increased activation of ChCs for one week caused elongation of the AIS and increased expression of $Na_v1.6$ at the AIS. These morphological and molecular changes were consistent with a decreased AP threshold and increased intrinsic excitability of PNs. This suggest that the persistent increase of inhibition to the AIS induced homeostatic changes in the PNs, resulting in an increase in excitability to balance the excessive inhibition. Therefore, chronic alterations in ChC to AIS connection bidirectionally induced homeostatic changes in PN excitability by tuning the AIS structure and $Na_v1.6$ expression.

Alterations in somatic inhibition does not elicit structural changes of the AIS

We next sought to investigate whether other forms of inhibitory input might induce the same homeostatic changes in the AIS. Parvalbumin (PV) fast-spiking interneurons are the main source of perisomatic inhibition in the cortex (*49*). Traditionally, ChCs and PV basket cells are thought to be the two major subtypes of PV fast-spiking interneurons, with ChCs targeting the AIS and PV basket cells targeting the soma. Therefore, we set out to investigate whether chronic manipulation of PV basket cells might have any effect on AIS plasticity. Although both ChCs and basket cells are believed to express PV as a biomarker, recent single-cell RNA sequencing data have revealed that ChCs can be further grouped into PV-high and PV-low subtypes (*34, 50*). Therefore, we set out to determine the properties of ChCs in the PL region. First, we crossed the *PV-Flp* driver line with the *Unc5b-CreER* driver line and the intersectional reporter line, *Ai65*, to label the PV-positive ChCs (*Unc5b-CreER:PV-Flp:Ai65*). Interestingly, few tdTomato-positive cells were shown in the mPFC, suggesting that most ChCs in the mPFC are the PV-low subtype (Fig. 5A). To corroborate this observation, we performed immunohistochemistry with anti-PV antibody in the *Unc5b-CreER:Nkx2.1-Flp:Ai65* brain slices. Consistent with what we found in the *Unc5b-CreER:PV-Flp:Ai65* line, the expression level of PV was hardly detectable in the ChCs in the FL and IL region, confirming that the majority of ChCs in the PL region are the PV-low subtype (Fig. 5B and 5C). These findings provide us with an opportunity to differentially manipulate PV basket cells and ChCs in this area, thus further dissecting their functional differences.

To determine whether bidirectional manipulations of PV basket cells had any effect on AIS plasticity, we virally expressed Cre-dependent DIO-hM3Dq or DIO-EGFP in the PL region of *PV-Cre* mice (Fig. 5D). Two weeks later, we verified the effectiveness of CNO on PV basket cells. Whole-cell patch recordings showed that CNO application increased the activity of PV basket cells expressing hM3Dq (fig. S9). Then, CNO was applied intraperitoneally for 7 days to achieve chronic activation of PV basket cells (Fig. 5D). Chronic activation of PV basket cells for 7 days did not alter the length of the AIS or the expression of $Na_v1.6$ in the PL region (Fig. 5E to 5G). In line with these results, the blockage of synaptic transmission from PV basket cells by expressing Tettox did not induce the changes in AIS length or AIS $Na_v1.6$ expression at 4 weeks p.i. (Fig. 5H-5K). In addition, there were no observed alterations in the expression of somatic $Na_v1.6$ channels (fig. S10). These results indicate that chronic alteration of somatic inhibition from PV basket cells is not sufficient to induce plastic changes in the PN AIS, signifying a requirement of direct synaptic input from ChCs.

Behavioral deficits caused by blocking ChC transmission is reversed when AIS plasticity occurs

To test whether homeostatic plasticity induced by changes in AIS input from ChCs could manifest in animal behaviors that are controlled by the PL PNs, we performed a set of behavioral tests. Although PL PNs have been implied in many behavioral paradigms, we chose to prioritize social behavior. This is because PL PNs has been consistently shown to have a negative impact on social behavior (*51-53*). Additionally, it is a behavioral paradigm that does not require extensive training, and thereby would not introduce other forms of plasticity that may interact or interfere the homeostatic plasticity we focused on.

We took advantage of the time course of homeostatic changes by virally blocking axo-axonic synaptic transmission in the PL region and conducted social behavioral test at 2, 3 and 4 weeks p.i. (Fig. 6A, 6B, and fig. S11). We first assessed whether blocking ChC

transmission would have an immediate effect on social behavior when the homeostatic plasticity had not occurred yet. At 2 weeks p.i., the Tettox-expressing group showed less interest in socializing with stranger mice (Fig. 6C-6F). The ratio of interaction time in the stranger box versus object box was reduced in the Tettox group compared with control group (Fig. 6D and 6E). Furthermore, the total social time was significantly less in the Tettox group (Fig. 6F). In the social novelty test, the Tettox-expressing mice were equally driven to the novel stranger as the control mice (Fig. 6D). These data indicate that the acute inhibition of ChC to PN connections in the PL region leads to impairments in social ability. This aligns with previous reports that have shown similar deficits in social behavior following the activation of PL PNs or the inhibition of other types of inhibitory neurons in the same region (*51, 54, 55*). At 3 weeks p.i., when the PN excitability remained unchanged, the social deficits remained (fig. S11). However, at 4 weeks p.i., when homeostatic plasticity had occurred, the social deficits were recovered (Fig. 6G to 6J). We observed a slightly increased ratio of interaction time in the stranger box versus object box (Fig. 6H and 6I), but the total social time did not differ between the two groups (Fig. 6J). In another word, the deficits in sociability observed at 2 weeks p.i. were reserved at 4 weeks p.i., which is consistent with the timing of homeostatic plasticity occurring in the PL PNs. No changes in motor deficits or anxiety-related behavior were observed (fig. S12). These results suggest that the reduced inhibitory input from ChCs was counteracted by the decreased excitability of PL PNs, which relieved their negative impact on social behavior (*51, 54*).

We next explored whether the homeostatic plasticity induced by enhancement of ChC activity could also work in a similar way. We bilaterally injected AAV-DIO-hM3Dq or DIO-EGFP (as control) into PL region of *Unc5b-CreER* mice, followed by TMX induction 2 days later (Fig. 7A and 7B). First, we tested whether acute activation of PL ChCs would elicit any changes in social behavior. CNO was applied to animals 30 minutes before the behavioral test to achieve acute activation (Fig. 7A). We found that mice with acute enhancement of ChC activity displayed a significant increase in the time spent in the social box without any changes in their mobility, indicating that acute activation of ChCs had a prosocial effect (Fig. 7C-7F, and fig. S13). The saline (SAL) groups were also included as control groups, and no significant difference was found between the EGFP-SAL group and hM3Dq-SAL group (fig. S14). Next, we examined whether the increased excitability of PL PNs could potentially counteract the prosocial effect mediated by activating ChCs. We performed the social test after chronic activation of ChCs for 7 consensus days (Fig. 7A). Unlike acute activation, mice with chronic activation of ChCs showed normal social ability compared with the control group (Fig. 7G-7J). The interaction time ratio of stranger mice and the total social time showed no difference between the chronic activation group and the control group (Fig. 7I and 7J). Similarly, the social novelty test showed no significant difference (Fig. 7H).

Taken together, our findings suggest that acute and chronic alterations of ChC input lead to different outcomes in social behavior, which align with the timing of plastic changes in the AIS. These observations highlight the importance of homeostatic plasticity originated from the AIS of the PL PNs. This mechanism may enable the animal to adapt to abnormal axo-axonic synaptic input, allowing for the restoration of appropriate behavior (Fig. 8). However, the excessive sociability of the Tettox group suggested an over-compensatory effect, indicating the importance of an intact microcircuit in maintaining normal animal behavior.

Discussion

Previous studies have shown that alterations of network activity cause homeostatic rearrangement of PN AIS(*11, 12, 19*). Plastic changes of the AIS effectively adjust the properties of AP firing and propagation, which in turn oppose ongoing deviations of activity levels and stabilize network functions. Here, we extended these studies by investigating AIS plasticity responding to changes in ChC synaptic input. We found that chronic alterations of synaptic input to the AIS by blocking axo-axonic synaptic transmission or by pharmacogenetic enhancement of ChCs induced structural and functional changes of the AIS. Altered AIS structure and expression levels of voltage-gated sodium channel correlated with shifted initiation threshold of AP, which were reflected by changes in neuronal excitability. These homeostatic plastic changes observed in the PL PNs counteract the alterations in inhibitory input on the AIS. Since the activity of the PL PNs is tightly associated with social behavior (*51, 54*), acute activation and inactivation of ChC inhibitory input to the PL PNs changed social behavior bidirectionally. However, these effects were diminished upon chronic manipulation of ChCs and were consistent with the timing of homeostatic plasticity occurring in the PL PNs. This suggests that the homeostatic changes originating from the AIS serve to counteract the altered inhibitory input and enable the animal to adapt to disruptions in specific neuronal signaling. Our results provide evidence for input-specific regulation of AIS plasticity and its contribution to compensatory changes in disturbed functional microcircuits.

It is worth noting that the synaptic plasticity in ChCs also follows a homeostatic rule, depending on the polarity of axo-axonic synapses (*47*). Modulation of PN activity in the somatosensory cortex effectively adjust the innervation of ChCs to the PN AISs, with opposite direction observed between early developmental stage (P12-P18) when GABA is depolarizing at the AIS, and young adulthood (P40-P46) when GABA is hyperpolarizing. Recent studies have suggested that GABAergic input to the AIS inhibits AP generation across the switch in GABA synapse polarity, even when GABA is depolarizing (*48*). These seemingly contradictory results raise the question of whether manipulating ChC during early developmental stages would induce homeostatic plasticity in the AIS towards the opposite direction or not. In Dr. Burrone's study, axo-axonic synapse plasticity can be driven in a cell-autonomous manner (*47*). However, pharmacogenetic activation of ChCs during early developmental stages (P12-P18, when GABA is depolarizing) did not lead to a significant change in AIS length of the innervated PNs (*47*). There might be several explanations: First, it is possible that the effect of GABA on the AIS might be heterogenous during this developmental stage. In Dr. Burrone's work, 35% depolarizing, 24% hyperpolarizing and 41% putative shunting were shown at P12-P18 (*47*). The heterogeneity suggests that the response of AIS might be a mixture. Another possibility is that during development, the AIS undergoes dynamic changes, and the length of the AIS becomes more stable after P21(*19*). Therefore, it is plausible that activity is only one of the mechanisms regulating AIS structure during early developmental stages, and other intrinsic developmental programs may also contribute. Testing these possibilities would require further investigation.

ChCs are an interneuron subtype identified only in mammals so far and are located solely in the neocortex or allocortex, but not in other brain areas (*56*). Our findings that the AISs of cortical PNs adapt to direct synaptic input to the AIS suggest that PNs in the cortex might possess a strategic adjustment capacity that subcortical neurons lack. Our previous findings showed that mPFC ChCs preferentially innervate PNs projecting to basal lateral amygdala ($_{BLA}$PNs) over those projecting to the contralateral prelimbic cortex ($_{cPL}$PNs)(*27, 57*). In the territory of a single ChC axonal collateral, around 80% $_{BLA}$PNs are innervated, whereas around 60% for $_{cPL}$PNs are innervated (*57*). Meanwhile, cartridges on the AIS of $_{BLA}$PNs

harbor significantly more boutons than those of on the $_{cPL}$PNs, indicating that the AISs of $_{BLA}$PNs receive more ChC input than those of $_{cPL}$PNs (*57*). This finding poses the possibility that the AISs of different cortical PN subtypes might have varying degrees of response to local synaptic input. It is worth our future endeavor to further dissect the cell-type-specific features of AIS plasticity.

Interneurons can actively control the synaptic plasticity of cortical PNs(*58-60*). Plasticity of local inhibitory circuits is critical to excitatory neurons during experience-dependent plasticity and learning(*20, 61-65*). Subtype-specific alterations is believed to be able to control synaptic plasticity at subcellular resolution (*61*). However, prolonged changes in interneuron activity could trigger postsynaptic excitatory neuron hyperactive, and homeostatic regulation is necessary to safeguard proper circuit functions. Here we show that enhanced activation of ChCs, but not PV basket cells, induces the structural alteration of the AIS of excitatory neuron. It is important to note that, changes in global activity at a greater magnitude than activating locally infected PV basket cells, as those induced by adding high concentration of K^+ in the *in vitro* neuronal cultures or altered sensory input (*11, 12, 19, 21*), could also induce plastic changes in the AIS. However, such subcellular-domain specific homeostatic mechanism allows the cells to adjust themselves in a more sophisticated manner on top of those responding to more generic changes in network activity. We speculate that homeostatic regulations operate not only under generic changes of network activity but also under activity changes in specific microcircuits.

The lack of observed plastic changes in AISs of PNs after manipulating PV basket cells in our experimental setup may have several explanations. One possibility is that AIS-specific inputs may be a much more potent driver to induce structural and functional homeostatic changes in this subcellular domain. Another possibility is that ChCs and PV basket cells exhibit significant differences in their local microcircuits (*27, 66-68*). ChCs specifically target the AIS of PNs in the PL region, whereas PV basket cells innervate multiple cell types, including PNs, PV basket cell themselves, and ChCs (*27, 67, 68*). This complex local circuit involving multiple cell types may exert reciprocal control mechanisms and maintain a delicate balance within local circuit, which may not necessarily manifest as changes in PN excitability. Previous reports have focused on how interneurons adapt network activity to act as local homeostats (*69, 70*), whereas our work suggests that interneuron subtype initiates plastic changes of PN AIS, providing an appealing idea that homeostatic plasticity happens at the subcellular level when microcircuit activity is disturbed.

Intact mPFC cortical neuronal excitatory and inhibitory balance is critical for higher cognitive functions(*54*). Compromises in mPFC cortical inhibition are often found in animal models of autism or schizophrenia (*71-73*). While homeostatic plasticity may regulate various functions associated with PL region when the balance is disrupted, we prioritized social behavior as a functional measure of homeostatic plasticity in our specific context. This choice is made as social behavior is a behavior paradigm that does not require an extensive training process before behavioral test. This minimizes the introduction of other types of plasticity that may occur during learning process and could complicate the interpretation of the results. Additionally, it is well-established that the activity of PL PN has a negative impact on social behavior, and GABAergic inputs, from either PV basket neurons or SST neurons, can relieve their inhibitory effect on social behavior (*51, 54, 55, 74*). Since PL PNs are the only postsynaptic targets of the ChCs in the PL region, it is reasonable to expect that other behaviors associated with PL PN may also be affected by

ChC manipulation. However, whether the disruptions of these behaviors may also be regulated by homeostatic rules would require further investigation.

The nervous system's ability to adapt to various perturbations is crucial for maintaining normal brain functions. Our study has shown that social behavior is impaired after acutely blocking ChC synaptic transmission in the PL region. However, these behavioral deficits are reversed when AIS plasticity occurs, suggesting that intrinsic homeostatic plasticity is a key component for maintaining normal animal behavior. In line with our observation, several genetic mouse models of ASD have demonstrated impaired intrinsic homeostatic plasticity (*75-77*). In addition, studies have reported a decrease in ChC count, but not PV-basket cell count, in the mPFC region of individuals with ASD, further highlighting the critical role of ChC and AIS-homeostasis in its pathology (*78*). Nonetheless, further research is needed to determine whether the loss of AIS plasticity in response to altered ChC activity contributes to the etiology of ASD and other brain disorders.

Together, the results presented here support the idea that disturbance of subtype-specific inhibitory input can drive homeostatic plasticity of PNs at the subcellular level. Prolonged alteration of axo-axonic synaptic input induced structural and functional plasticity of the AIS, which contributed to the tuning of neuronal excitability. Future studies are required to explore whether other subcellular structures of PNs undergo homeostatic plasticity after the disturbance of subtype-specific inhibitory input and whether they contribute to stabilizing normal brain functions.

Materials and Methods

Animals

All procedures were conducted in accordance with the protocols approved by the Institutional Animal Care and Use Committee of Fudan University. *Unc5b-CreER* and *Nkx2.1-Flp* were provided by Z.J. Huang (Duke University School of Medicine), while *PV-Cre* (JAX Stock 008069), *PV-FlpE* (JAX Stock 021191), and *Rosa26-loxpSTOPloxp-frtSTOPfrt-tdTomato* (*Ai65*, JAX Stock 021875) were from Jackson Laboratory. *Tau-loxpSTOPloxp-frtSTOPfrt-DTR* (*Tau-ds-DTR*) was acquired from M. Goulding (Salk Institute). To specifically label ChCs, we combined *Unc5b-CreER* driver with *Nkx2.1-Flp* and the *Ai65* intersectional reporter. Ablation of ChCs was achieved by crossing *Unc5b-CreER:Nkx2.1-Flp:Ai65* with *Tau-ds-DTR*. Genetic labeling of PV-positive ChCs was done by crossing *Unc5b-CreER* and *PV-Flp* with *Ai65* reporter line. Wild-type C57BL/6j mice (from Charles River, Shanghai, China) were used as stranger mice in 3-chamber social test. Timed-pregnant female CD1 mice (Charles River) were used for E14.5 *in utero* electroporation experiments targeting PNs in mPFC. All mice were maintained under standard conditions of 20 °C–24 °C, 40%–60% relative humidity, and a 12-hour light/dark cycle, with food and water freely available. The age of animals used ranged from P30 to P63. Mice of both sexes were used in all experiments except for the behavioral tests, in which only male mice were used.

DNA Constructs

The gRNA targeting sequence of mouse *Scn8a* (C-terminus) is as follows: 5'-TTACCCTCTCCTCTAGCACT-3'. The gRNA sequence was inserted into PX330 backbone (gift from Dr. Feng Zhang, plasmid #42230, RRID: Addgene_42230), which

contains hSpCas9 and the gRNA backbone. The DNA donor carrying the HA-epitope was obtained from the pHiUGE HA-epitope donor ORF1 (referenced from Dr. Scott Soderling, plasmid #200372, RRID: Addgene_200372)(*79*). This donor construct includes a donor-specific gRNA that guides Cas9-mediated self-cleavage, resulting in the release of the HA encoding sequence for non-homogenous genomic insertion at the *Scn8a* site.

Tamoxifen induction

Tamoxifen (Sigma-Aldrich, MO, USA) was dissolved in corn oil (20 mg/ml) at room temperature by ultrasonication. Stocks were stored at 4°C for no more than 1 month. Tamoxifen was administered intraperitoneally twice, at a dose of 2 mg per 20 g body weight. For labeling or ablating ChCs, *Unc5b-CreER:Nkx2.1-Flp:Ai65* or *Unc5b-CreER:Nkx2.1-Flp:Ai65:Tau-ds-DTR* mice were injected at P21 and P23; for *Unc5b-CreER* mice infected with either AAV-tetanus toxin or AAV-hM3Dq, tamoxifen administration was done at P30 and P32.

Ablation and activation of ChCs

To ablate ChCs for histochemical studies, the expression of DTR in ChCs was induced by intraperitoneally injecting TMX into *Unc5b-CreER:Nkx2.1-Flp:Ai65:Tau-ds-DTR* mice at P21 and P23. Then, diphtheria toxin (DT, 50 μg/kg; Sigma-Aldrich, MO, USA) was intraperitoneally injected at P37 and P39. Histochemical experiments were performed 7 days after DT injection. Clozapine N-oxide (CNO, 0.6 mg/kg; Sigma-Aldrich, MO, USA) was intraperitoneally injected twice a day for 7 days from P46 to P53 to chronically activate ChCs in *Unc5b-CreER* mice infected with AAV-hM3Dq.

***In Utero* Electroporation and Stereotaxic surgery**

In utero electroporation was performed flowing previously established protocols, with modifications to target L2/3 neurons in the mPFC region. Briefly, timed-pregnant *Unc5b-CreER* mouse at E14.5 was anesthetized using 2% isoflurane with an air flow rate of 0.8L/min. The utero horns were exposed, and a DNA solution containing a mixture of PX330-sg*Scn8a*, pHiUGE HA-epitope donor, and pCAG-YFP with final concentrations of 1 μg/μl, 1 μg/μl, and 0.2 μg/μl, respectively, was manually injected into the lateral ventricle of the embryos using a glass micropipette. The positive pole of the electrode was positioned at the frontal-dorsal region of the embryonic forebrain to direct the DNA towards the progenitor cells of the prefrontal cortex. Electric pulses (40V; 50ms) were administered five times at 1 s intervals. Following electroporation, the uterus was carefully repositioned, and the wound was closed using surgical sutures.

Standard surgical procedures were used for stereotaxic injection, as previously described (*27*). Briefly, animals were anesthetized with isoflurane inhalation (1.5% in a mixture with oxygen, applied at 1.0 L/min) and head-fixed in the stereotaxic apparatus. Viruses were injected into medial prefrontal cortex (mPFC), particularly in PL region, at 4 weeks of age, using the coordinates referenced to the Paxinos and Watson Mouse Brain in Stereotaxic Coordinates, 3rd edition: anteroposterior (AP): 1.94 mm; mediolateral (ML): ± 0.25 mm; dorsoventral (DV): -1.7 mm. For each injection site, a total volume of 200 nL of virus was injected at ~100 nL/min, controlled by hand. The following adeno-associated viral vectors were used to express genes of interest in a Cre-recombinase-dependent manner: AAV2/9-hEF1a-DIO-mCherry-P2A-Tettox-WRPE-pA (6.13×10^{11} vg/ml; Taitool, Shanghai, China);

pAAV-hSyn-DIO-hM3Dq-EGFP (8.45 × 10^{11} vg/ml; Genechem, Shanghai, China); AAV2/9-hSyn-FLEX-EGFP-WPRE-pA (3.28 × 10^{11} vg/ml; Taitool, Shanghai, China); AAV2/9-hSyn-FLEX-tdTomato-WPRE-pA (9.85×10^{10} vg/ml, Taitool, Shanghai, China); AAV2/9-CamKIIa-hChR2(E123A)-eYFP-WPRE-pA (1×10^{13} vg/ml, Taitool, Shanghai, China). For immunohistochemical experiments, to minimize the impact of batch effects, AAV virus expressing fluorescent proteins (control) and the ones expressing Tettox or hM3Dq were injected unilaterally in the same mouse but on different sides. For behavioral tests, bilateral injection was applied to achieve robust delivery in ChCs in the PL region.

Immunohistochemistry

Animals were anesthetized with isoflurane inhalation (3%) and perfused transcardially with PBS and 4% paraformaldehyde (PFA) in 0.1 mol/L phosphate buffer. The brains were post fixed in 4% PFA in 0.1 mol/L phosphate buffer overnight at 4 °C and then dehydrated with 30% sucrose in PBS. Coronal sections at a thickness of 50 μm were prepared using a vibratome (Leica, VT1000S, Wetzlar, Germany). Before incubation with the primary antibody, the brain sections were subjected to antigen retrieval by water bath at 85°C for 15 min in retrieval buffer (25 mmol/L Tris-HCl, pH 8.5; 1 mmol/L EDTA, 0.05% SDS). After cooling to RT, the sections were washed in PBS for 10 min. Immunohistochemistry was performed as previously described (*80*). Briefly, the sections were blocked with 10% newborn goat serum (NGS) and 0.3% Triton X-100 in PBS at RT for 1 h, followed by incubation in primary antibodies diluted in 3% NGS and 0.3% Triton X-100 in PBS overnight at 4 °C. The following primary antibodies were used: rabbit anti-RFP (1:10000; Rockland, PA, USA); chicken IgY anti-GFP (1:10000; Aves Labs.Inc, CA, USA); mouse IgG1 anti-Pan Na_v 1 (1:100; N419/78; Millipore, MA, USA), mouse IgG1 anti- Na_v 1.6 (1:100; K87A/10; NeuroMab, CA, USA); mouse IgG1 anti-gephyrin (1:500; mAb7a; Synaptic Systems, Coventry, UK); guinea pig anti-VGAT (1:500; Synaptic Systems, Coventry, UK); mouse IgG2a anti-AnkyrinG (1:500; N106/36; Millipore, MA, USA); mouse IgG1 anti-parvalbumin (1:500; PVALB-19; Sigma-Aldrich, MO, USA); mouse IgG1 anti-VAMP2 (1:500; Synaptic Systems, Coventry, UK). After three washes with PBS for 10 min each, the secondary antibodies were applied for 2 h at RT. The secondary antibodies used were (all from Thermo Fisher Scientific, MA, USA): Alexa Fluor (AF) 488 goat anti-mouse IgG1 (1:1000), AF 488 goat anti-mouse IgG2a (1:1000), AF 488 goat anti-guinea pig (1:1000), DyLight 488 goat anti-chicken, AF 555 goat anti-rabbit (1:1000), AF 555 goat anti-mouse IgG1 (1:1000), AF 555 goat anti-mouse IgG2a (1:1000), AF 647 goat anti-mouse IgG2a (1:1000), and AF 647 goat anti-mouse IgG1 (1:1000). The same wash steps were applied after incubation. The brain slices were then mounted onto microscope slides for image acquisition.

Image acquisition and analysis

Images were acquired from Nikon AX confocal laser scanning microscope (Nikon, Tokyo, Japan) with 10× air-immersion or 60× oil-immersion objective. Images for immunochemical analysis were captured at a resolution of 2048 × 2048 pixels using a Z-series to cover the entire AIS with a depth interval of 0.55 mm. The analysis of AIS was used and modified as previously described (*11, 57*). In brief, the fluorescence profile of AISs were obtained from Fiji (https://fiji.sc/). For each intact AIS, a 3-pixel-wide line was drawn through and past the fluorescence signal of Ankyrin-G in the 60× stacked images when a custom-made Fiji marco (https://github.com/Mojackhak/AIS) was recording the pixel intensity of all z-series slices along the line. The data were import to the MatLab to

reconstruct the AIS-containing plane including the AIS profile in the z-direction and gain the 3D profile by the modified published code (*11*). The proximal and distal position of the AIS was identified through the normalized fluorescence intensity of Ankyrin-G dropped below 0.33. The distance of AIS from soma was calculated as the distance between the soma boundary and the proximal position of the AIS. The width of the AIS was recorded at the proximal position of the AIS. The intensity normalization formula is as follows: normalized intensity of the pixel = (pixel intensity − minimum intensity) / (maximum intensity − minimum intensity). For analysis of VGAT and Gephyrin, puncta were manually counted following each single z-plane image of the entire AIS by using Fiji. IMARIS 7.5.2 were used for extraction of VGAT and Gephyrin puncta overlapping with AIS. The AIS were reconstructed with the "create surface" tool. Threshold value were calculated for all slices using the "above automatic threshold" tool.

Slice preparation and electrophysiological recordings

The slice preparation and electrophysiological recordings were conducted following previously described methods (*57*). Briefly, mice were anesthetized using isoflurane before decapitation. The mouse brain was rapidly removed and transferred to ice-cold, oxygenated artificial cerebrospinal fluid (section ACSF) (in mmol/L: 110 choline chloride, 2.5 KCl, 4 $MgSO_4$, 1 $CaCl_2$, 1.25 NaH_2PO_4, 26 $NaHCO_3$, 11 D-glucose, 10 sodium ascorbate, 3.1 sodium pyruvate, pH 7.35, 300 mOsm) for 1 min. Coronal prefrontal cortical slices, 250 µm–300 µm thick, containing the medial prefrontal cortex (mPFC), were cut at 1 °C–2 °C using a vibratome (Leica VT1200S, Wetzlar, Germany). Subsequently, the slices were allowed to recover and were incubated in oxygenated ACSF (in mmol/L: 124 NaCl, 2.5 KCl, 2 $MgSO_4$, 2 $CaCl_2$, 1.25 NaH_2PO_4, 26 $NaHCO_3$, 11 d-glucose, pH 7.35, 300 mOsm) at 34°C for 30 minutes, and then stayed in room temperature before the slice was transferred into the recording chamber. Whole-cell patch recordings were performed in L2 of the mPFC, with L1/2 border and the slice shape as visual landmarks based on the atlas (Paxinos and Watson, Mouse Brain in Stereotaxic Coordinates, 3rd edition). The patch pipette recording solution contained the following components (in mmol/L): 147 potassium gluconate, 3 KCl, 10 sodium phosphocreatine, 10 HEPES, 4 ATP·Mg, 0.3 Na_2GTP, and 0.3 EGTA. The pH of the solution was adjusted to 7.25 with KOH, and the osmolarity was maintained between 290 mOsm and 300 mOsm.

Whole-cell patch recordings was performed from L2 PNs in the dorsal mPFC, using Axopatch 700B amplifiers (Molecular Devices, Union City, CA). Slices were visualized using an Olympus Bx51 microscope equipped with infrared-differential interference contrast optics (IR-DIC) and a fluorescence excitation source. Throughout the recordings, the chamber was continuously perfused with oxygenated working ACSF at a temperature range of 33°C to 34°C. The recorded PNs with triangle cell body were mainly in the upper L2 (close to L1/2 border), which were supposed to be the main distribution area of ChC axons(*27*). During voltage-clamp mode, the membrane potential was held at -75 mV for the resistance test, while in current-clamp mode, zero holding current was applied without correcting for the junction potential for the resting membrane potential examination. The steps of current square injection with 600 ms duration were employed to examine the firing rates versus current injections. The first action potential (AP) in the trial evoking 4-10 APs was analyzed. The threshold of an AP was determined as the voltage at which the derivative of the membrane potential (dV/dt) reached 20 mV/ms and was calculated using MATLAB's spline interpolation function (*5*). During the recording, the pipette capacitance was neutralized with 3.00 pF. The series resistance (Rs) was monitored and the cells with Rs <

15 MΩ were accepted. The recorded signals were low-pass filtered at 3 kHz, digitized at 80 kHz using a Digidata 1550B digitizer (Molecular Devices), and subsequently analyzed using pClamp 10.7 software (Molecular Devices) and custom-made MATLAB code.

To preserve the transmembrane Cl^- gradient, we performed cell-attached voltage-clamp recordings to monitor the spike activity of ChR2-expressing PNs. Wide-field light pulses at a wavelength of 473 nm (2-5 ms in duration) were delivered to activate PNs. The patch pipettes, filled with ACSF, had impedance ranging from 4-6 MΩ. Sharp glass pipettes, filled with 200mM GABA (pH = 5), were used for iontophoresis and had an impedance of 60-100 MΩ. During GABA iontophoresis, a constant holding current of -10 nA was applied to prevent GABA leakage, while positive current pulses (150 nA, 20 ms) were used to induce iontophoresis of GABA. We added 25 μM DL-AP5 (NMDA receptor antagonist) and 10 μM NBQX (AMPA receptor antagonist) and 50 μM CGP55845 ($GABA_B$ receptor antagonist) to the bath solution to block fast glutamatergic synaptic transmission and $GABA_B$ receptor inhibitory effect, respectively. Current signals were amplified using a Multiclamp 700B amplifier (Molecular Devices) and sampled by a Power3 1401 (Cambridge Electronic Design, CED) together with Spike2 software (Version 8, CED). The signals were recorded at 50 kHz and filtered with Bessel filter at 10 kHz.

Behavior assays

The behavior assays were conducted between 10:00 am and 5:00 pm. All subject mice were male and randomly grouped. To minimize stress, all mice were handled for 5 min on 5 consecutive days prior to test day to acclimation to moderate handling. On the test day, the mice were placed in the test room to acclimate to the environment for 30 minutes before the test. At the end of each test, the testing apparatus was scrubbed twice with 75% alcohol and ddH_2O. Mouse trajectories were recorded and analyzed using Toxtrac (https: //toxtrac.sourceforge.io). Acute pharmacogenetic activation of ChCs during the behavior assay was achieved by i.p. injection of CNO (1mg/kg) approximately 30 minutes before the test, while chronic activation of ChCs was achieved by i.p. injection twice a day for 8 consecutive days.

Social interaction assays

The social testing apparatus comprises a three-chamber Perspex box, with each chamber measuring 60 cm in length, 40 cm in width, and 44 cm in height. The two adjacent chambers are separated by a freely removable baffle. On the day of testing, the subject mouse was placed in the central chamber and allowed to freely explore the empty apparatus for 10 minutes. Empty social boxes were then placed on either side of the apparatus, and the subject mice were allowed to explore them for 10 minutes. In the social ability test, a strange mouse of the same sex and age was randomly placed in one social box, and an object was placed in the social box on the other side. The subject mouse was then allowed to investigate freely for 10 min. In the social novelty test, the object in the social box was replaced with another strange mouse, followed by a 10 min investigation by the subject mouse. We defined a circular area within 5 cm around the social box as the interaction zone and considered the time spent around the interaction zone as interaction time. The degree of preference of a stranger mouse over the object represented the subject's social ability. The social index was calculated using the following formula: (interaction time with stranger – interaction time with object) / total test time. For the social novelty test, the formula was modified as follows: (interaction time with new mice – interaction time with old mice) / total test time.

Open-field test

The mice were placed in a plexiglass box measuring 42 cm × 42 cm × 50 cm for 10 minutes to allow for free exploration. Motor performance was quantified by calculating the average speed and total distance traveled. The time spent in the center of the box (half of the box area) was also recorded.

Elevated plus maze (EPM) test

The EPM apparatus was elevated 73 cm above the floor and consisted of a 6 cm × 6 cm center section, two open arms (35 cm × 6 cm), and two closed arms (35 cm × 6 cm × 19 cm). To assess anxiety-related behavior, the subject mouse was placed in the center section with its head on one side of the open arms, followed by 5 minutes of free exploration. The time spent on the open arms was then recorded.

Statistical analysis

Statistical analyses and data plots were performed using GraphPad Prism 9 software (GraphPad). All data are presented as mean ± SEM. Unpaired two-tail Student's *t*-tests were used to compare two groups. Two-way ANOVA followed by appropriate post-hoc corrections was used to compare AP firing frequency and normalized mean fluorescence intensity along AISs (details are given in the respective figure legend). Unpaired multiple *t* test with Holm-Sidak method was used to compare the time course of Tettox and social index. Statistical significance was defined as $^{*}P < 0.05$, $^{**}P < 0.01$, $^{***}P < 0.001$, or $^{****}P < 0.0001$. Values of $P \geq 0.05$ were considered not significantly different. All figures were composed using Illustrator software (Adobe Systems, USA).

References

1. K. Eichel, T. Uenaka, V. Belapurkar, R. Lu, S. Cheng, J. S. Pak, C. A. Taylor, T. C. Sudhof, R. Malenka, M. Wernig, E. Ozkan, D. Perrais, K. Shen, Endocytosis in the axon initial segment maintains neuronal polarity. *Nature* **609**, 128-135 (2022).
2. M. Kuijpers, D. van de Willige, A. Freal, A. Chazeau, M. A. Franker, J. Hofenk, R. J. Rodrigues, L. C. Kapitein, A. Akhmanova, D. Jaarsma, C. C. Hoogenraad, Dynein Regulator NDEL1 Controls Polarized Cargo Transport at the Axon Initial Segment. *Neuron* **89**, 461-471 (2016).
3. J. M. Sobotzik, J. M. Sie, C. Politi, D. Del Turco, V. Bennett, T. Deller, C. Schultz, AnkyrinG is required to maintain axo-dendritic polarity in vivo. *Proc Natl Acad Sci U S A* **106**, 17564-17569 (2009).
4. M. N. Rasband, The axon initial segment and the maintenance of neuronal polarity. *Nat Rev Neurosci* **11**, 552-562 (2010).
5. W. Hu, C. Tian, T. Li, M. Yang, H. Hou, Y. Shu, Distinct contributions of Na(v)1.6 and Na(v)1.2 in action potential initiation and backpropagation. *Nat Neurosci* **12**, 996-1002 (2009).
6. D. Zhou, S. Lambert, P. L. Malen, S. Carpenter, L. M. Boland, V. Bennett, AnkyrinG is required for clustering of voltage-gated Na channels at axon initial segments and for normal action potential firing. *J Cell Biol* **143**, 1295-1304 (1998).
7. M. H. Kole, S. U. Ilschner, B. M. Kampa, S. R. Williams, P. C. Ruben, G. J. Stuart, Action potential generation requires a high sodium channel density in the axon initial segment. *Nat Neurosci* **11**, 178-186 (2008).
8. M. H. Kole, G. J. Stuart, Signal processing in the axon initial segment. *Neuron* **73**, 235-247 (2012).
9. K. J. Bender, L. O. Trussell, The physiology of the axon initial segment. *Annu Rev Neurosci* **35**, 249-265 (2012).
10. M. D. Evans, A. S. Dumitrescu, D. L. H. Kruijssen, S. E. Taylor, M. S. Grubb, Rapid Modulation of Axon Initial Segment Length Influences Repetitive Spike Firing. *Cell Rep* **13**, 1233-1245 (2015).

11. M. S. Grubb, J. Burrone, Activity-dependent relocation of the axon initial segment fine-tunes neuronal excitability. *Nature* **465**, 1070-1074 (2010).
12. H. Kuba, Y. Oichi, H. Ohmori, Presynaptic activity regulates Na(+) channel distribution at the axon initial segment. *Nature* **465**, 1075-1078 (2010).
13. A. Fekete, N. Ankri, R. Brette, D. Debanne, Neural excitability increases with axonal resistance between soma and axon initial segment. *Proc Natl Acad Sci U S A* **118**, (2021).
14. E. Lazarov, M. Dannemeyer, B. Feulner, J. Enderlein, M. J. Gutnick, F. Wolf, A. Neef, An axon initial segment is required for temporal precision in action potential encoding by neuronal populations. *Sci Adv* **4**, eaau8621 (2018).
15. B. Zonta, A. Desmazieres, A. Rinaldi, S. Tait, D. L. Sherman, M. F. Nolan, P. J. Brophy, A critical role for Neurofascin in regulating action potential initiation through maintenance of the axon initial segment. *Neuron* **69**, 945-956 (2011).
16. K. J. Bender, L. O. Trussell, Axon initial segment Ca2+ channels influence action potential generation and timing. *Neuron* **61**, 259-271 (2009).
17. G. G. Turrigiano, The Self-Tuning Neuron: Synaptic Scaling of Excitatory Synapses. *Cell* **135**, 422-435 (2008).
18. M. S. Grubb, Y. Shu, H. Kuba, M. N. Rasband, V. C. Wimmer, K. J. Bender, Short- and long-term plasticity at the axon initial segment. *J Neurosci* **31**, 16049-16055 (2011).
19. N. Jamann, D. Dannehl, N. Lehmann, R. Wagener, C. Thielemann, C. Schultz, J. Staiger, M. H. P. Kole, M. Engelhardt, Sensory input drives rapid homeostatic scaling of the axon initial segment in mouse barrel cortex. *Nat Commun* **12**, 23 (2021).
20. K. Seignette, N. Jamann, P. Papale, H. Terra, R. O. Porneso, L. de Kraker, C. van der Togt, M. van der Aa, P. Neering, E. Ruimschotel, P. R. Roelfsema, J. S. Montijn, M. W. Self, M. H. P. Kole, C. N. Levelt, Experience shapes chandelier cell function and structure in the visual cortex. *Elife* **12**, (2024).
21. N. Akter, R. Fukaya, R. Adachi, H. Kawabe, H. Kuba, Structural and Functional Refinement of the Axon Initial Segment in Avian Cochlear Nucleus during Development. *J Neurosci* **40**, 6709-6721 (2020).
22. R. Yamada, H. Kuba, Structural and Functional Plasticity at the Axon Initial Segment. *Frontiers in Cellular Neuroscience* **10**, (2016).
23. S. A. Buffington, M. N. Rasband, The axon initial segment in nervous system disease and injury. *Eur J Neurosci* **34**, 1609-1619 (2011).
24. P. Somogyi, A specific 'axo-axonal' interneuron in the visual cortex of the rat. *Brain Res* **136**, 345-350 (1977).
25. B. Dudok, M. Szoboszlay, A. Paul, P. M. Klein, Z. Liao, E. Hwaun, G. G. Szabo, T. Geiller, B. Vancura, B. S. Wang, S. McKenzie, J. Homidan, L. M. F. Klaver, D. F. English, Z. J. Huang, G. Buzsaki, A. Losonczy, I. Soltesz, Recruitment and inhibitory action of hippocampal axo-axonic cells during behavior. *Neuron* **109**, 3838-3850 e3838 (2021).
26. J. Szabadics, C. Varga, G. Molnar, S. Olah, P. Barzo, G. Tamas, Excitatory effect of GABAergic axo-axonic cells in cortical microcircuits. *Science* **311**, 233-235 (2006).
27. J. Lu, J. Tucciarone, N. Padilla-Coreano, M. He, J. A. Gordon, Z. J. Huang, Selective inhibitory control of pyramidal neuron ensembles and cortical subnetworks by chandelier cells. *Nat Neurosci* **20**, 1377-1383 (2017).
28. B. Compans, J. Burrone, Chandelier cells shine a light on the formation of GABAergic synapses. *Curr Opin Neurobiol* **80**, 102697 (2023).
29. Y. Zhu, R. L. Stornetta, J. J. Zhu, Chandelier cells control excessive cortical excitation: characteristics of whisker-evoked synaptic responses of layer 2/3 nonpyramidal and pyramidal neurons. *J Neurosci* **24**, 5101-5108 (2004).
30. K. Jung, M. Chang, A. Steinecke, B. Burke, Y. Choi, Y. Oisi, D. Fitzpatrick, H. Taniguchi, H. B. Kwon, An adaptive behavioral control motif mediated by cortical axo-axonic inhibition. *Nat Neurosci*, (2023).
31. M. B. Perumal, B. Latimer, L. Xu, P. Stratton, S. Nair, P. Sah, Microcircuit mechanisms for the generation of sharp-wave ripples in the basolateral amygdala: A role for chandelier interneurons. *Cell Rep* **35**, 109106 (2021).

32. L. Gong, X. Liu, J. Wu, M. He, Emerging strategies for the genetic dissection of gene functions, cell types, and neural circuits in the mammalian brain. *Mol Psychiatry* **27**, 422-435 (2022).
33. R. Raudales, G. Kim, S. M. Kelly, J. Hatfield, W. Guan, S. Zhao, A. Paul, Y. Qian, B. Li, Z. J. Huang, Specific and comprehensive genetic targeting reveals brain-wide distribution and synaptic input patterns of GABAergic axo-axonic interneurons. *bioRxiv*, (2023).
34. A. Paul, M. Crow, R. Raudales, M. He, J. Gillis, Z. J. Huang, Transcriptional Architecture of Synaptic Communication Delineates GABAergic Neuron Identity. *Cell* **171**, 522-539 e520 (2017).
35. H. Taniguchi, J. Lu, Z. J. Huang, The spatial and temporal origin of chandelier cells in mouse neocortex. *Science* **339**, 70-74 (2013).
36. M. Inan, J. Welagen, S. A. Anderson, Spatial and temporal bias in the mitotic origins of somatostatin- and parvalbumin-expressing interneuron subgroups and the chandelier subtype in the medial ganglionic eminence. *Cereb Cortex* **22**, 820-827 (2012).
37. B. Duan, L. Cheng, S. Bourane, O. Britz, C. Padilla, L. Garcia-Campmany, M. Krashes, W. Knowlton, T. Velasquez, X. Ren, S. Ross, B. B. Lowell, Y. Wang, M. Goulding, Q. Ma, Identification of spinal circuits transmitting and gating mechanical pain. *Cell* **159**, 1417-1432 (2014).
38. K. L. Hedstrom, Y. Ogawa, M. N. Rasband, AnkyrinG is required for maintenance of the axon initial segment and neuronal polarity. *J Cell Biol* **183**, 635-640 (2008).
39. A. Fréal, N. Jamann, J. Ten Bos, J. Jansen, N. Petersen, T. Ligthart, C. C. Hoogenraad, M. H. P. Kole, Sodium channel endocytosis drives axon initial segment plasticity. *Science Advances* **9**, (2023).
40. E. Katz, O. Stoler, A. Scheller, Y. Khrapunsky, S. Goebbels, F. Kirchhoff, M. J. Gutnick, F. Wolff, I. A. Fleidervish, Role of sodium channel subtype in action potential generation by neocortical pyramidal neurons. *Proceedings of the National Academy of Sciences of the United States of America* **115**, E7184-E7192 (2018).
41. C. Tian, K. Wang, W. Ke, H. Guo, Y. Shu, Molecular identity of axonal sodium channels in human cortical pyramidal cells. *Front Cell Neurosci* **8**, 297 (2014).
42. M. Royeck, M. T. Horstmann, S. Remy, M. Reitze, Y. Yaari, H. Beck, Role of axonal NaV1.6 sodium channels in action potential initiation of CA1 pyramidal neurons. *J Neurophysiol* **100**, 2361-2380 (2008).
43. H. Liu, H. G. Wang, G. Pitt, Z. Liu, Direct Observation of Compartment-Specific Localization and Dynamics of Voltage-Gated Sodium Channels. *Journal of Neuroscience* **42**, 5482-5498 (2022).
44. M. Prinz, S. Jung, J. Priller, Microglia Biology: One Century of Evolving Concepts. *Cell* **179**, 292-311 (2019).
45. X. Chen, D. A. Wolfe, D. S. Bindu, M. Zhang, N. Taskin, D. Goertsen, T. F. Shay, E. E. Sullivan, S. F. Huang, S. Ravindra Kumar, C. M. Arokiaraj, V. M. Plattner, L. J. Campos, J. K. Mich, D. Monet, V. Ngo, X. Ding, V. Omstead, N. Weed, Y. Bishaw, B. B. Gore, E. S. Lein, A. Akrami, C. Miller, B. P. Levi, A. Keller, J. T. Ting, A. S. Fox, C. Eroglu, V. Gradinaru, Functional gene delivery to and across brain vasculature of systemic AAVs with endothelial-specific tropism in rodents and broad tropism in primates. *Nat Commun* **14**, 3345 (2023).
46. G. Rinetti-Vargas, K. Phamluong, D. Ron, K. J. Bender, Periadolescent Maturation of GABAergic Hyperpolarization at the Axon Initial Segment. *Cell Rep* **20**, 21-29 (2017).
47. A. Pan-Vazquez, W. Wefelmeyer, V. Gonzalez Sabater, G. Neves, J. Burrone, Activity-Dependent Plasticity of Axo-axonic Synapses at the Axon Initial Segment. *Neuron* **106**, 265-276 e266 (2020).
48. A. M. Lipkin, K. J. Bender, Axon Initial Segment GABA Inhibits Action Potential Generation throughout Periadolescent Development. *J Neurosci* **43**, 6357-6368 (2023).
49. A. Kepecs, G. Fishell, Interneuron cell types are fit to function. *Nature* **505**, 318-326 (2014).
50. A. Chen, Y. Sun, Y. Lei, C. Li, S. Liao, J. Meng, Y. Bai, Z. Liu, Z. Liang, Z. Zhu, N. Yuan, H. Yang, Z. Wu, F. Lin, K. Wang, M. Li, S. Zhang, M. Yang, T. Fei, Z. Zhuang, Y. Huang, Y. Zhang, Y. Xu, L. Cui, R. Zhang, L. Han, X. Sun, B. Chen, W. Li, B. Huangfu, K. Ma, J. Ma, Z. Li, Y. Lin, H. Wang, Y. Zhong, H. Zhang, Q. Yu, Y. Wang, X. Liu, J. Peng, C. Liu, W. Chen, W. Pan, Y. An, S. Xia, Y. Lu, M. Wang, X. Song, S. Liu, Z. Wang, C. Gong, X. Huang, Y. Yuan, Y. Zhao, Q. Chai, X. Tan, J. Liu, M. Zheng, S. Li, Y. Huang, Y. Hong, Z. Huang, M. Li, M. Jin, Y. Li, H. Zhang, S. Sun, L. Gao, Y. Bai, M. Cheng, G. Hu, S. Liu, B. Wang, B. Xiang, S. Li, H. Li, M. Chen, S. Wang, M. Li, W. Liu, X. Liu, Q. Zhao, M. Lisby, J. Wang, J. Fang, Y. Lin, Q. Xie, Z. Liu, J. He, H.

Xu, W. Huang, J. Mulder, H. Yang, Y. Sun, M. Uhlen, M. Poo, J. Wang, J. Yao, W. Wei, Y. Li, Z. Shen, L. Liu, Z. Liu, X. Xu, C. Li, Single-cell spatial transcriptome reveals cell-type organization in the macaque cortex. *Cell* **186**, 3726-3743 e3724 (2023).

51. W. C. Huang, A. Zucca, J. Levy, D. T. Page, Social Behavior Is Modulated by Valence-Encoding mPFC-Amygdala Sub-circuitry. *Cell Rep* **32**, (2020).
52. M. Murugan, H. J. Jang, M. Park, E. M. Miller, J. Cox, J. P. Taliaferro, N. F. Parker, V. Bhave, H. Hur, Y. P. Liang, A. R. Nectow, J. W. Pillow, I. B. Witten, Combined Social and Spatial Coding in a Descending Projection from the Prefrontal Cortex. *Cell* **171**, 1663-+ (2017).
53. M. Sato, N. Nakai, S. Fujima, K. Y. Choe, T. Takumi, Social circuits and their dysfunction in autism spectrum disorder. *Molecular Psychiatry*, (2023).
54. O. Yizhar, L. E. Fenno, M. Prigge, F. Schneider, T. J. Davidson, D. J. O'Shea, V. S. Sohal, I. Goshen, J. Finkelstein, J. T. Paz, K. Stehfest, R. Fudim, C. Ramakrishnan, J. R. Huguenard, P. Hegemann, K. Deisseroth, Neocortical excitation/inhibition balance in information processing and social dysfunction. *Nature* **477**, 171-178 (2011).
55. L. Liu, H. F. Xu, J. Wang, J. Li, Y. Y. Tian, J. Q. Zheng, M. He, T. L. Xu, Z. Y. Wu, X. M. Li, S. M. Duan, H. Xu, Cell type-differential modulation of prefrontal cortical GABAergic interneurons on low gamma rhythm and social interaction. *Science Advances* **6**, (2020).
56. A. Howard, G. Tamas, I. Soltesz, Lighting the chandelier: new vistas for axo-axonic cells. *Trends Neurosci* **28**, 310-316 (2005).
57. A. Hu, R. Zhao, B. Ren, Y. Li, J. Lu, Y. Tai, Projection-Specific Heterogeneity of the Axon Initial Segment of Pyramidal Neurons in the Prelimbic Cortex. *Neurosci Bull*, (2023).
58. R. Hattori, K. V. Kuchibhotla, R. C. Froemke, T. Komiyama, Functions and dysfunctions of neocortical inhibitory neuron subtypes. *Nat Neurosci* **20**, 1199-1208 (2017).
59. J. J. Letzkus, S. B. Wolff, A. Luthi, Disinhibition, a Circuit Mechanism for Associative Learning and Memory. *Neuron* **88**, 264-276 (2015).
60. Y. Fu, M. Kaneko, Y. Tang, A. Alvarez-Buylla, M. P. Stryker, A cortical disinhibitory circuit for enhancing adult plasticity. *Elife* **4**, e05558 (2015).
61. S. X. Chen, A. N. Kim, A. J. Peters, T. Komiyama, Subtype-specific plasticity of inhibitory circuits in motor cortex during motor learning. *Nat Neurosci* **18**, 1109-1115 (2015).
62. E. Abs, R. B. Poorthuis, D. Apelblat, K. Muhammad, M. B. Pardi, L. Enke, D. Kushinsky, D. L. Pu, M. F. Eizinger, K. K. Conzelmann, I. Spiegel, J. J. Letzkus, Learning-Related Plasticity in Dendrite-Targeting Layer 1 Interneurons. *Neuron* **100**, 684-699 e686 (2018).
63. Y. Fu, J. M. Tucciarone, J. S. Espinosa, N. Sheng, D. P. Darcy, R. A. Nicoll, Z. J. Huang, M. P. Stryker, A cortical circuit for gain control by behavioral state. *Cell* **156**, 1139-1152 (2014).
64. D. Kim, H. Jeong, J. Lee, J. W. Ghim, E. S. Her, S. H. Lee, M. W. Jung, Distinct Roles of Parvalbumin- and Somatostatin-Expressing Interneurons in Working Memory. *Neuron* **92**, 902-915 (2016).
65. S. Krabbe, E. Paradiso, S. d'Aquin, Y. Bitterman, J. Courtin, C. Xu, K. Yonehara, M. Markovic, C. Muller, T. Eichlisberger, J. Grundemann, F. Ferraguti, A. Luthi, Adaptive disinhibitory gating by VIP interneurons permits associative learning. *Nat Neurosci* **22**, 1834-1843 (2019).
66. K. Zhang, B. H. Ren, Y. L. Tai, J. T. Lyu, Distinct recruitment dynamics of chandelier cells and basket cells by thalamocortical inputs. *Sheng Li Xue Bao* **74**, 697-704 (2022).
67. M. Galarreta, S. Hestrin, Electrical and chemical synapses among parvalbumin fast-spiking GABAergic interneurons in adult mouse neocortex. *Proceedings of the National Academy of Sciences of the United States of America* **99**, 12438-12443 (2002).
68. V. Szegedi, M. Paizs, J. Baka, P. Barzo, G. Molnar, G. Tamas, K. Lamsa, Robust perisomatic GABAergic self-innervation inhibits basket cells in the human and mouse supragranular neocortex. *Elife* **9**, (2020).
69. D. van Versendaal, R. Rajendran, M. H. Saiepour, J. Klooster, L. Smit-Rigter, J. P. Sommeijer, C. I. De Zeeuw, S. B. Hofer, J. A. Heimel, C. N. Levelt, Elimination of inhibitory synapses is a major component of adult ocular dominance plasticity. *Neuron* **74**, 374-383 (2012).
70. S. H. Lee, P. W. Land, D. J. Simons, Layer- and cell-type-specific effects of neonatal whisker-trimming in adult rat barrel cortex. *J Neurophysiol* **97**, 4380-4385 (2007).

71. K. K. Cho, R. Hoch, A. T. Lee, T. Patel, J. L. Rubenstein, V. S. Sohal, Gamma rhythms link prefrontal interneuron dysfunction with cognitive inflexibility in Dlx5/6(+/-) mice. *Neuron* **85**, 1332-1343 (2015).
72. S. Han, C. Tai, R. E. Westenbroek, F. H. Yu, C. S. Cheah, G. B. Potter, J. L. Rubenstein, T. Scheuer, H. O. de la Iglesia, W. A. Catterall, Autistic-like behaviour in Scn1a+/- mice and rescue by enhanced GABA-mediated neurotransmission. *Nature* **489**, 385-390 (2012).
73. W. Cao, S. Lin, Q. Q. Xia, Y. L. Du, Q. Yang, M. Y. Zhang, Y. Q. Lu, J. Xu, S. M. Duan, J. Xia, G. Feng, J. Xu, J. H. Luo, Gamma Oscillation Dysfunction in mPFC Leads to Social Deficits in Neuroligin 3 R451C Knockin Mice. *Neuron* **98**, 670 (2018).
74. A. Selimbeyoglu, C. K. Kim, M. Inoue, S. Y. Lee, A. S. O. Hong, I. Kauvar, C. Ramakrishnan, L. E. Fenno, T. J. Davidson, M. Wright, K. Deisseroth, Modulation of prefrontal cortex excitation/inhibition balance rescues social behavior in CNTNAP2-deficient mice. *Sci Transl Med* **9**, (2017).
75. V. Tatavarty, A. T. Pacheco, C. G. Kuhnle, H. Lin, P. Koundinya, N. J. Miska, K. B. Hengen, F. F. Wagner, S. D. Van Hooser, G. G. Turrigiano, Autism-Associated Shank3 Is Essential for Homeostatic Compensation in Rodent V1. *Neuron* **106**, 769-+ (2020).
76. J. P. K. Ip, I. Nagakura, J. Petravicz, K. J. Li, E. A. C. Wiemer, M. Sur, Major Vault Protein, a Candidate Gene in 16p11.2 Microdeletion Syndrome, Is Required for the Homeostatic Regulation of Visual Cortical Plasticity. *Journal of Neuroscience* **38**, 3890-3900 (2018).
77. P. Bulow, T. J. Murphy, G. J. Bassell, P. Wenner, Homeostatic Intrinsic Plasticity Is Functionally Altered in Fmr1 KO Cortical Neurons. *Cell Rep* **26**, 1378-+ (2019).
78. J. Ariza, H. Rogers, E. Hashemi, S. C. Noctor, V. Martinez-Cerdeno, The Number of Chandelier and Basket Cells Are Differentially Decreased in Prefrontal Cortex in Autism. *Cereb Cortex* **28**, 411-420 (2018).
79. Y. Gao, E. Hisey, T. W. A. Bradshaw, E. Erata, W. E. Brown, J. L. Courtland, A. Uezu, Y. Xiang, Y. Diao, S. H. Soderling, Plug-and-Play Protein Modification Using Homology-Independent Universal Genome Engineering. *Neuron* **103**, 583-597 e588 (2019).
80. Y. Tai, J. A. Janas, C. L. Wang, L. Van Aelst, Regulation of chandelier cell cartridge and bouton development via DOCK7-mediated ErbB4 activation. *Cell Rep* **6**, 254-263 (2014).

Acknowledgments

We thank Dr. Martyn Goulding at the Salk Institute for the *Tau-DTR* mice and the Allen Brain Institute for the *Ai65* mice.

Funding:

National Natural Science Foundation of China grant 82071450 and 32371006(Y.T.)
National Natural Science Foundation of China grant 31970971 (M.H.)
National Natural Science Foundation of China grant 32371073 (J.L.)
National Science and Technology Innovation 2030 Major Projects of China STI2030-Major Projects-2022ZD0206500 (M.H.)
STI2030-Major Projects 2021ZD0202500 (Y.S.)
National Natural Science Foundation of China 32130044 and T2241002 (Y.S.)
National Natural Science Foundation of China 32200951 (Y.X.)
China Postdoctoral Science Foundation 2022M720801 (Y.X.)
US NIH NIH R01 MH094705-05 (Z.J.H.)

Author contributions:

Conceptualization: JL, YT
Methodology: RZ, BR, YX, AH, YQ, ZJH.
Investigation: RZ, BR, YX, JT, YZ
Visualization: RZ, JT, YZ, YQ, XX, YT
Supervision: YS, MH, JL, YT

Writing—original draft: RZ, YT
Writing—Review and editing: ZJH, YS, MH, JL, YT

Competing interests:
Authors declare that they have no competing interests.

Data and materials availability:
All data are available in the main text or the supplementary materials.

Figures and Tables

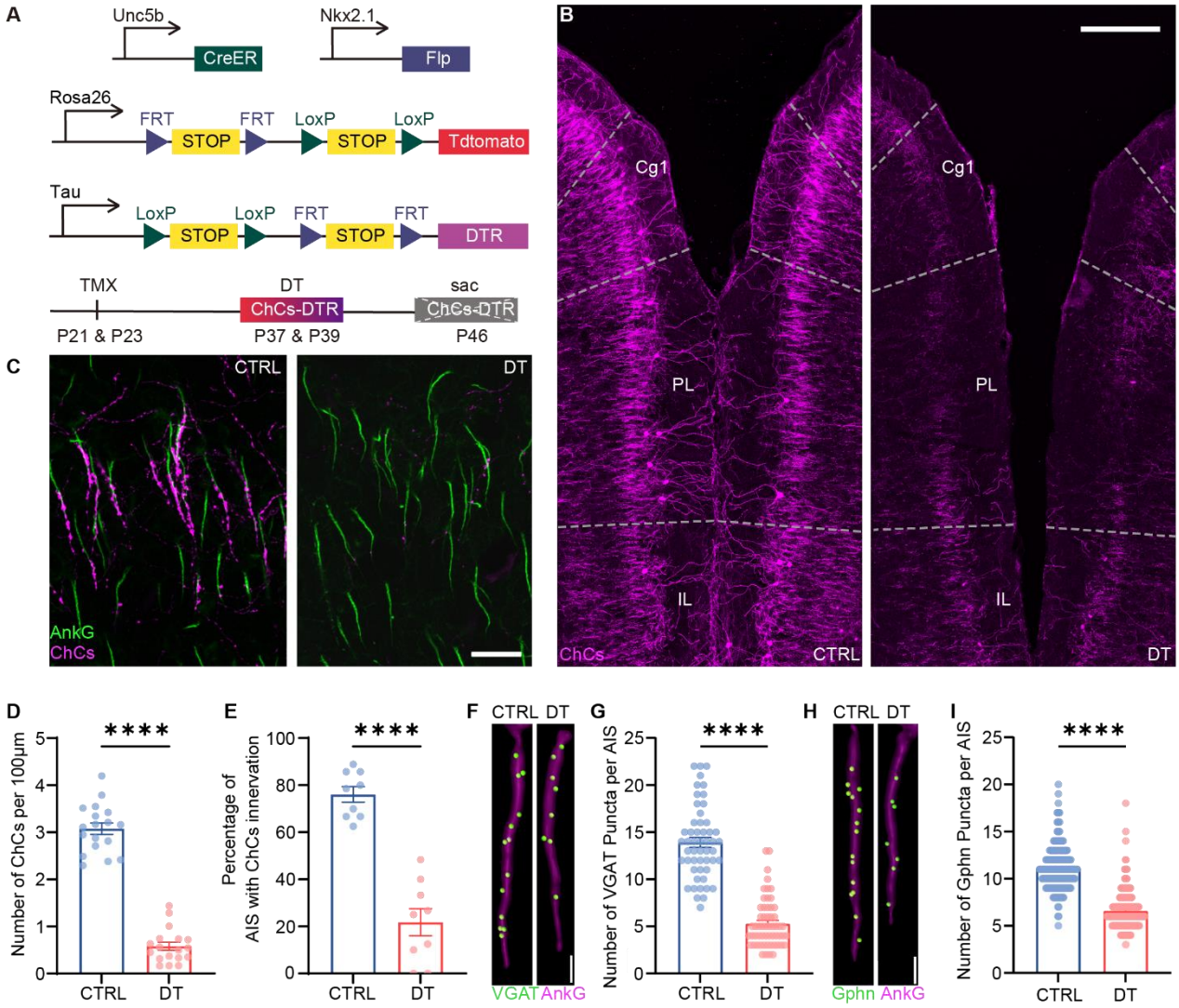

Fig. 1. Strategy to genetically ablate ChCs in vivo. (A) Schematic representation of the strategy of intersectional labeling (tdTomato) and ablation (*DTR*: diphtheria toxin receptor) of the ChCs. TMX was administered at P21 and P23 to induce *DTR* expression, following by i.p. injection of DT (diphtheria toxin) at P37 and P39. Animals were sacrificed one week later to assess ablation efficiency. **(B)** Representative images showing successful ablation of ChCs in the mPFC one week after DT injection. Scale bar: 200 µm **(C)** Representative images showing reduced innervation of the AISs by ChCs. Scale bar: 20 µm **(D)** Reduced number of ChCs per 100 µm located at the boundary of L1 and L2 after genetic ablation (CTRL: n = 18 brain slices, 3 mice; DT: n = 18 brain slices, 3 mice; P<0.0001, unpaired t-test). **(E)** Decreased overall percentage of L2/3 AISs innervated by ChC cartridges in the DT-treated group compared to the control group (CTRL: n = 9 brain slices, 3 mice; DT: n = 9 brain slices, 3 mice; P < 0.0001, unpaired t-test). **(F and G)** Reduction of VGAT puncta per AIS in ChC-ablated mice (CTRL: n = 52 cells, 3 mice; DT: n = 57 cells, 3 mice; P<0.0001, unpaired t-test). **(H and I)** Reduction of gephyrin puncta per AIS in ChC-ablated mice (CTRL: n = 224 cells, 3 mice; DT: n = 243 cells, 3 mice; P<0.0001, unpaired t-test). Data are represented as mean ± SEM. ****P < 0.0001.

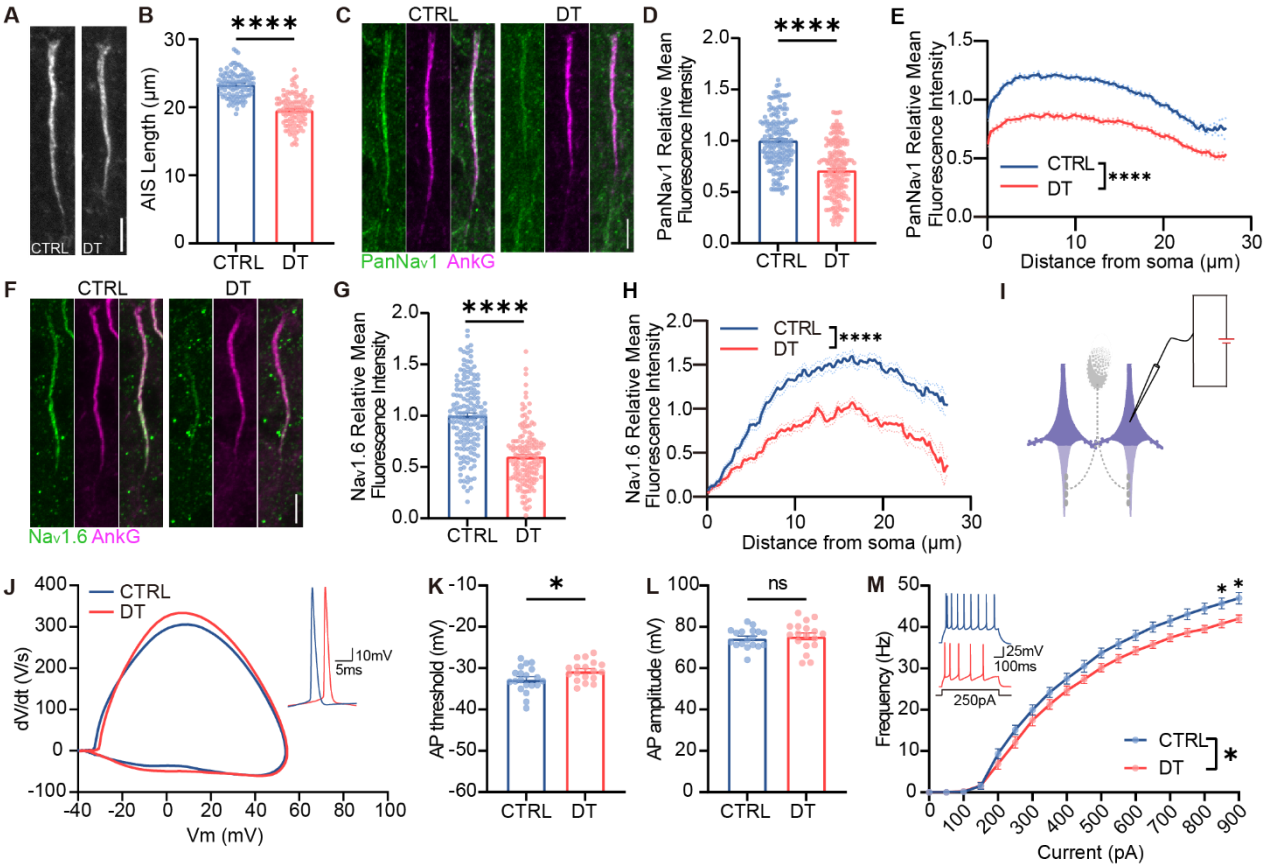

Fig. 2. Ablation of ChCs induced AIS structural changes and decreases neuronal excitability. **(A)** Representative images of L2 PN AIS without (CTRL) or with (DT) ChC ablation. Scale bar: 5 μm. **(B)** Reduced PN AIS length in DT group compared to control group (CTRL: n = 224 cells, 3 mice; DT: n = 243 cells, 3 mice; P < 0.0001, unpaired t-test). **(C)** Representative images of AIS with pan-Na_v1 staining. **(D-E)** Decreased mean fluorescence intensity of pan-Na_v1 **(D)** and normalized mean fluorescence intensity of pan-Na_v1 along AISs **(E)**. (CTRL: n = 173 cells, 3 mice; DT: n = 178 cells, 3 mice; P < 0.0001, unpaired t-test for **D**; P < 0.0001, two-way ANOVA for **E**). **(F)** Representative images of AIS with $Na_v1.6$ staining. **(G-H)** Decreased mean fluorescence intensity of Nav1.6 **(G)** and normalized mean fluorescence intensity of $Na_v1.6$ along AISs **(H)**. (CTRL: n = 159 cells, 3 mice; DT: n = 147 cells, 3 mice; P < 0.0001, unpaired t-test for **G**; P < 0.0001, two-way ANOVA for **H**). **(I)** Schematic illustrating whole-cell patch recording of L2 PNs innervated by ChCs. **(J)** Representative AP waveform (right) and phase plot (left). **(K)** Increased AP threshold after ChC ablation by DT. **(L)** No significant changes in AP amplitude (CTRL: n = 18 cells, 5 mice; DT: n = 18 cells, 6 mice; P = 0.029, unpaired t-test for **K**; P = 0.622, unpaired t-test for **L**). **(M)** Representative traces of AP trains elicited by current injection (left) and input/frequency relationship (right) as determined by injections of increasing currents. The DT-treated group showed significantly decreased firing frequency (CTRL: n = 32, 5 mice; DT: n = 26, 6 mice. two-way ANOVA, Sidak's multiple comparison test, P = 0.030). Data are represented as mean ± SEM. *P<0.05, ****P<0.0001.

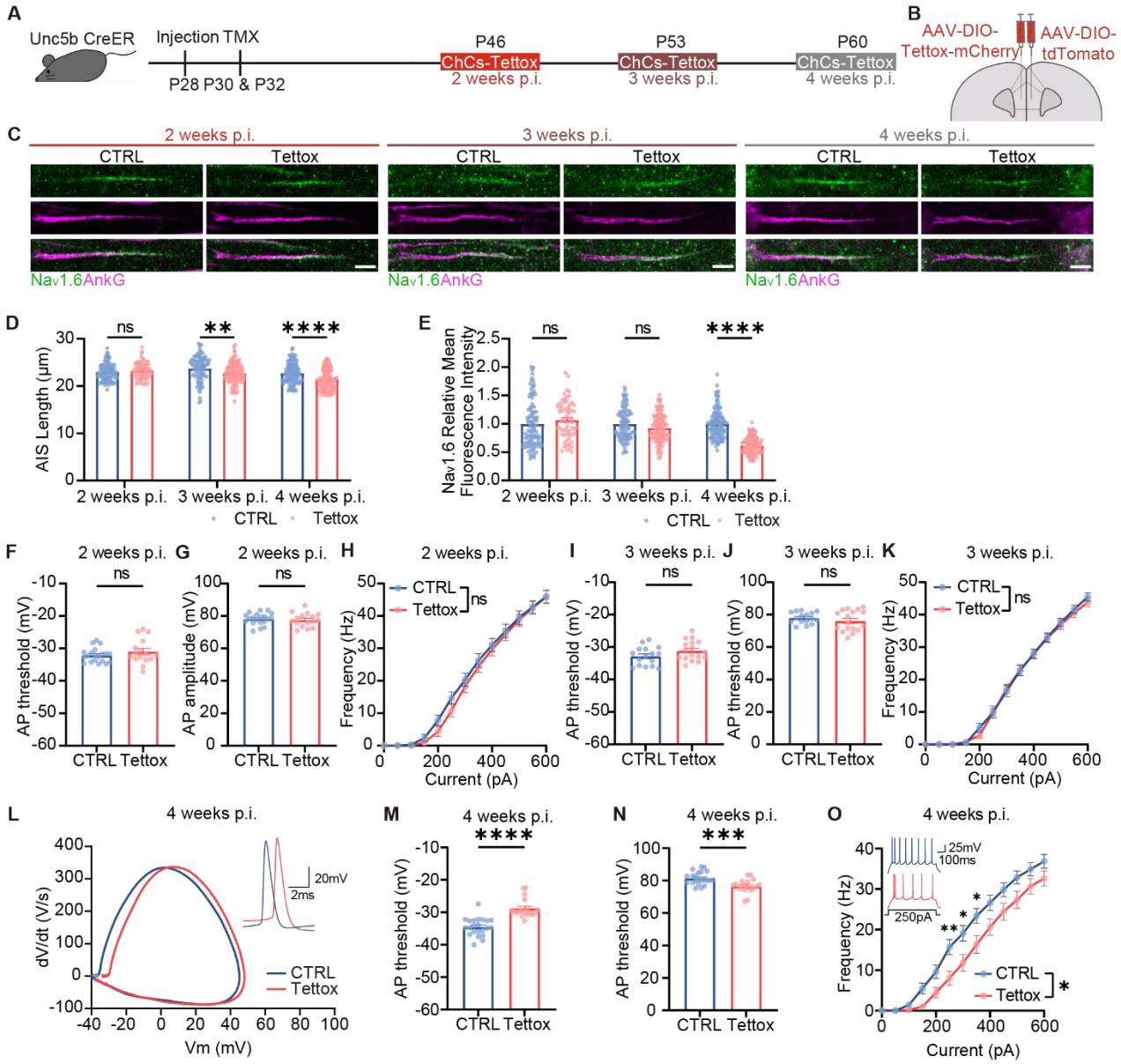

Fig. 3. Inactivation of axon-axonic neurotransmission leads to homeostatic changes of the PN AIS. (A) Schematic showing the time course of blocking ChC transmission strategy. **(B)** Schematic illustrating the viral injection strategy. **(C)** Representative images of immunostaining against Nav1.6 and AnkG at the indicated phases. Scale bar: 5 μm. **(D-E)** PN AIS length **(D)** and relative mean fluorescence intensity of $Na_v1.6$ **(E)** of the control group and Tettox group at the indicated phases. (2 weeks p.i.: CTRL: n = 101, Tettox: n = 62, P = 0.278 for AIS length, P = 0.276 for $Na_v1.6$ fluorescence intensity; 3 weeks p.i.: CTRL: n = 92, Tettox: n = 114, P = 0.007 for AIS length, P = 0.105 for $Na_v1.6$ fluorescence intensity; 4 weeks p.i.: CTRL: n = 121, Tettox: n = 121 cells, P < 0.0001 for both. Unpaired Holm-Sidak multiple t-test). **(F-K)** No significant changes in AP threshold **(F,I)**, AP amplitude **(G,J)**, and firing frequency **(H,K)** at 2 and 3 weeks p.i. (n = 16~22 cells from at least 3 mice; P > 0.05, unpaired t-test for **F,G,I,** and **J**; P > 0.05, two-way ANOVA for **H** and **K**.) **(L)** Representative AP waveform (right) and phase plot (left) at 4 weeks p.i. **(M-N)** Increased AP threshold **(M)** and decreased AP amplitude **(N)** after blocking axon-axonic synaptic transmission by Tettox at 4 weeks p.i. (CTRL: n = 22 cells, 4 mice; Tettox: n = 18 cells, 4 mice; P < 0.0001 for **M**, P < 0.001 for **N**, unpaired t-test). **(O)** The Tettox group showed significantly decreased firing frequency (CTRL: n = 26, 4 mice; Tettox: n = 26, 4 mice, P = 0.017, two-way ANOVA, Sidak's multiple comparison test, *P = 0.015 and 0.021, **P = 0.009). Data are represented as mean ± SEM. ns P>0.05, *P<0.05, ***P<0.001, ****P<0.0001.

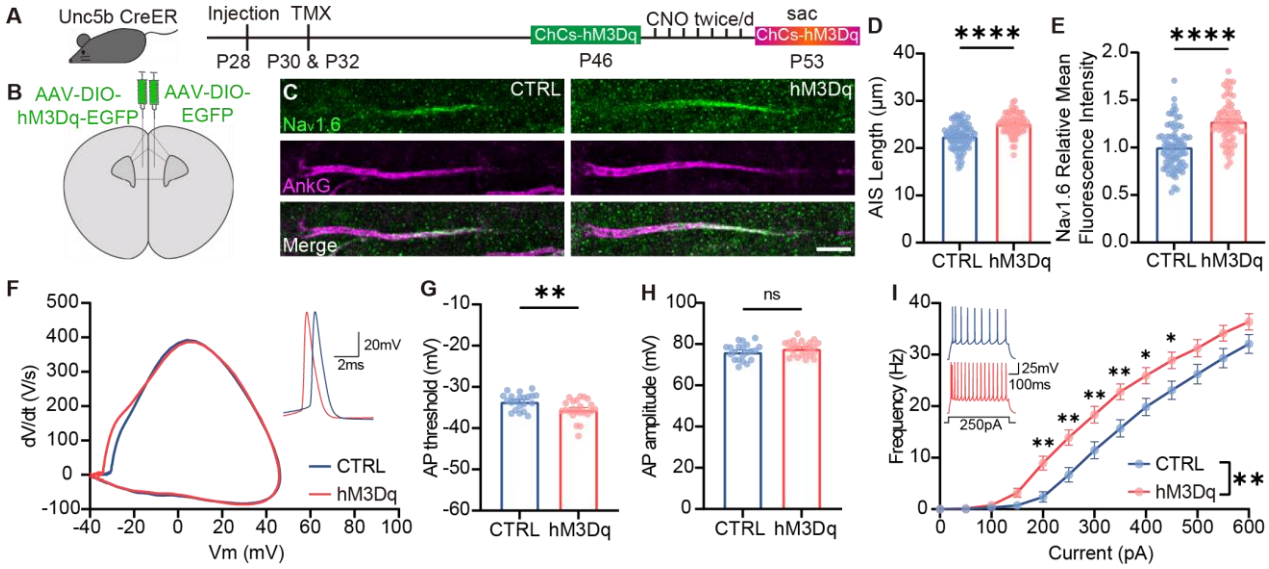

Fig. 4. Chronic pharmacogenetic activation of ChCs evoked homeostatic plasticity of PN AIS. **(A)** Schematic showing the strategy of chronic activation of ChCs. **(B)** Schematic illustrating the unilateral injection of AAV-DIO-hM3Dq-EGFP and AAV-DIO-EGFP in each hemisphere. **(C)** Representative images of immunostaining against $Na_v1.6$ and AnkG. Scale bar: 5 μm. **(D)** Increased PN AIS length in the hM3Dq group compared to the control group (CTRL: n =83 cells, 3 mice; hM3Dq: n = 68 cells, 3 mice; $P < 0.0001$, unpaired t-test). **(E)** Increased mean fluorescence intensity of $Na_v1.6$ after chronic activation of ChCs (CTRL: n = 83 cells, 3 mice; hM3Dq: n = 68 cells, 3 mice; $P < 0.0001$, unpaired t-test). **(F)** Representative AP waveform (right) and phase plot (left) of PNs in control and pharmacogenetic activated ChCs animals. **(G)** Decreased AP threshold after chronic activation of ChCs (CTRL: n = 21 cells, 5 mice; hM3Dq: n = 23 cells, 5 mice; P = 0.004, unpaired t-test). **(H)** No significant changes in AP amplitude between the control and hM3Dq group (CTRL: n = 21 cells, 5 mice; hM3Dq: n = 23 cells, 5 mice; P = 0.165, unpaired t-test). **(I)** Representative traces of AP trains elicited by current injection (left) and input/frequency relationship (right) as determined by injections of increasing currents. The hM3Dq group showed significantly increased firing frequency (CTRL: n = 28, 5 mice; Tettox: n = 34, 5 mice. P = 0.007, two-way ANOVA. Sidak's multiple comparison test, *P = 0.002 for 400 pA and 0.036 for 450 pA; **P = 0.0095 for 200 pA, 0.003 for 250 pA, 0.005 for 300 pA and 0.003 for 350 pA). Data are represented as mean ± SEM. ns $P > 0.05$, *$P < 0.05$, **$P < 0.01$****$P < 0.0001$.

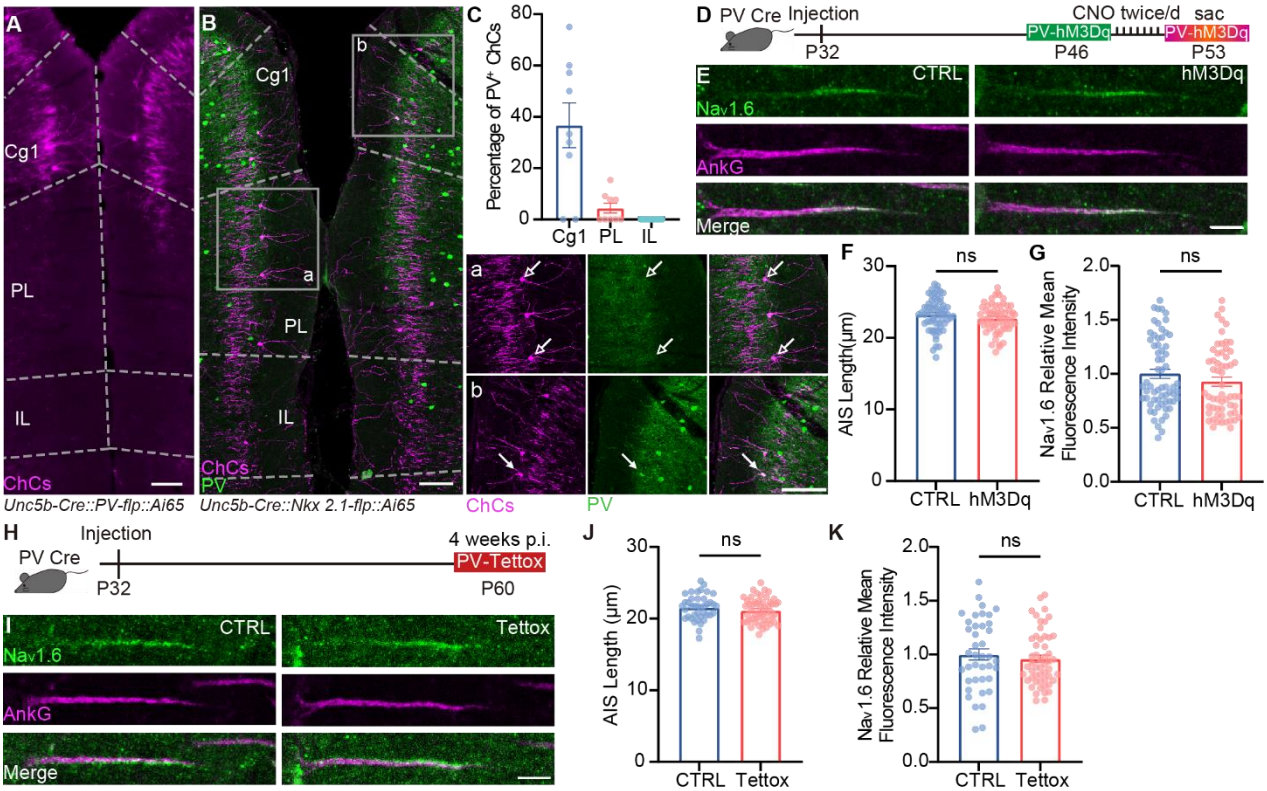

Fig. 5. Chronic manipulation of somatic inhibition failed to induce the plastic changes of the AIS. (A) Representative image showing that few ChCs were labeled in mPFC of *Unc5b-CreER; PV-Flp; Ai65* mouse. Scale bar: 100 μm. **(B)** Immunostaining of PV (green) in the *Unc5b-CreER; Nkx2.1-Flp; Ai65* mouse. Scale bar: 100 μm. Insets: hollow arrows indicate ChCs with low PV immunosignals; solid arrows indicate ChCs with high PV immunosignals. Scale bar: 100 μm. **(C)** Percentage of PV-positive ChCs versus total ChCs in Cg1, PL, and IL regions. **(D)** Schematic showing the strategy of chronic activation of PV basket cells. **(E)** Representative images of AIS stained with $Na_v1.6$ and AnkG antibodies. Scale bar: 5 μm. **(F)** No significant change in the AIS length (CTRL: n = 63 cells, 3 mice; hM3Dq: n = 58 cells, 3 mice; P = 0.228, unpaired t-test). **(G)** No significant change in the mean fluorescence intensity of $Na_v1.6$ after chronic activation of somatic inhibition (CTRL: n = 63 cells, 3 mice; hM3Dq: n = 58 cells, 3 mice; P = 0.174, unpaired t-test). **(H)** Schematic showing the strategy of chronic inhibition of PV basket cell synaptic transmission. Animals were sacrificed at 4 weeks p.i. at P60. **(I)** Representative images of AIS stained with $Na_v1.6$ (green) and AnkG (magenta) antibodies. Scale bar: 5 μm. **(J)** No significant change of the AIS length in the control group and Tettox group (CTRL: n = 40 cells, 3 mice; Tettox: n = 52 cells, 3 mice; P = 0.251, unpaired t-test). **(K)** No significant change in the mean fluorescence intensity of $Na_v1.6$ after chronic inhibition of PV basket cells (CTRL: n = 40 cells, 3 mice; Tettox: n = 52 cells, 3 mice; P = 0.512, unpaired t-test). Data are represented as mean ± SEM. ns P>0.05.

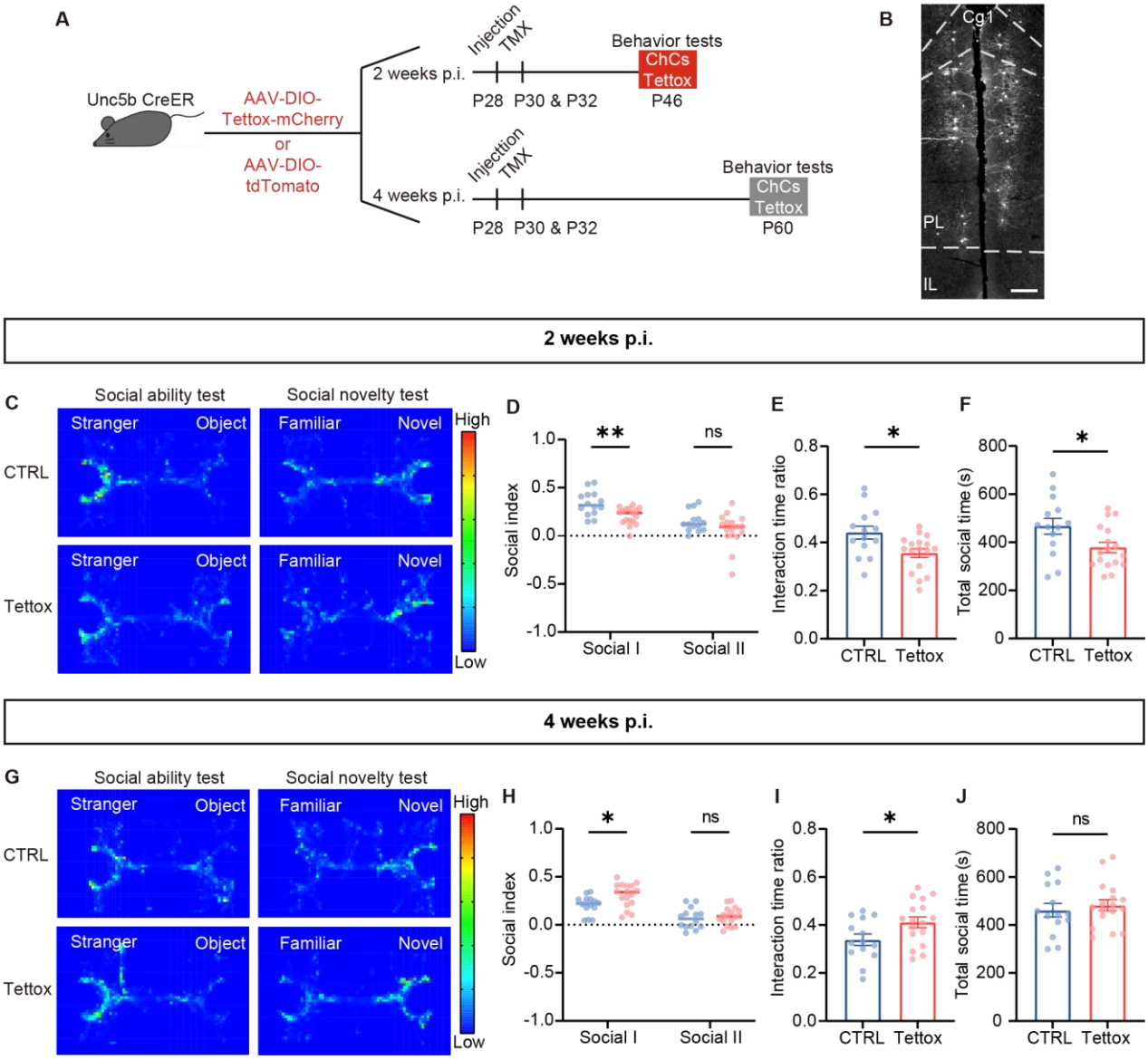

Fig. 6. Effect of reduced axon-axonic neurotransmission on social behavior. (A) Schematic showing the strategy of acute and chronic blocking of the PL ChC axon-axonic transmission. TMX was applied at P30 and P32 to induce Tettox expression in ChCs. Two weeks p.i. (P46) was defined as acute inhibition and 4 weeks p.i. (P60) was defined as chronic inhibition. **(B)** Representative image illustrating the injection site of AAV-DIO-Tettox. Scale bar: 200 µm. **(C)** Representative heatmaps of indicated groups in the acute inhibition condition. **(D)** Reduced preference in social approach but not social novelty test in the Tettox group in the acute condition (n = 14 for CTRL, n = 17 for Tettox, P = 0.005 for social ability, P = 0.121 for social novelty, unpaired Holm-Sidak multiple t-test). **(E-F)** Reduced interaction time ratio **(E)** and total social time **(F)** in Tettox group in the acute condition (n = 14 for CTRL, n = 17 for Tettox, P = 0.012 for exploration time ratio, P = 0.028 for total social time, unpaired t-test). **(G)** Representative heatmaps of indicated groups in the chronic inhibition condition. **(H)** Increased preference in social approach but not social novelty test in the Tettox group in the chronic condition. **(**n = 14 for CTRL, n = 17 for Tettox, P = 0.034 for social ability, P = 0.575 for social novelty, unpaired Holm-Sidak multiple t-test) **(I)** Increased interaction time ratio in the chronic Tettox group. (n = 14 for CTRL, n = 17 for Tettox, P = 0.033, unpaired t-test) **(J)** No change in total social time in the Tettox Group in the chronic condition (n = 14 for CTRL, n = 17 for Tettox, P = 0.569, unpaired t-test). Data are represented as mean ± SEM. ns $P > 0.05$, *$P < 0.05$, **$P < 0.01$.

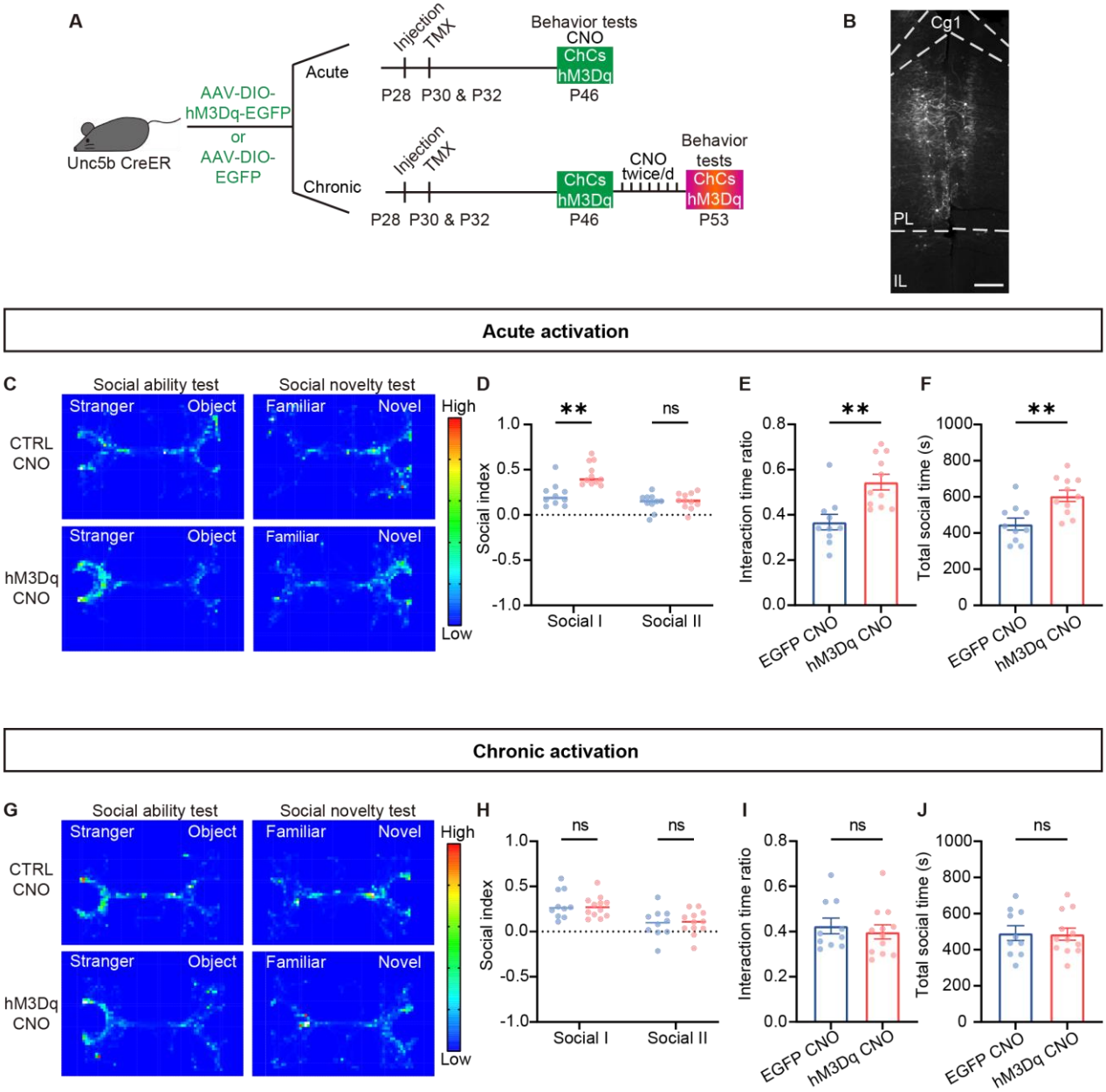

Fig. 7. Effect of pharmacogenetic activation of PL ChCs on social behavior. (A) Schematic showing the strategy of acute and chronic pharmacogenetic activation of the PL ChC axon-axonic transmission. AAV virus encoding DIO-hM3Dq-EGFP or DIO-EGFP was injected bilaterally at P28, TMX was applied at P30 and P32. Application of CNO started at two weeks p.i. when EGFP or hM3Dq was fully expressed (P46). Day 1 (P46) of CNO application was defined as acute activation of ChCs. Persistent CNO application twice a day for 7 days until P53 was defined as chronic activation of ChCs. **(B)** Representative image illustrating the injection site of AAV-DIO-hM3Dq. Scale bar: 200 µm. **(C)** Representative heatmaps of animals expressing AAV-DIO-EGFP or AAV-DIO-hM3Dq with acute activation of ChCs. **(D)** Increased preference in social approach but not social novelty test in the hM3Dq group after acute activation of ChCs (n = 10 for EGFP CNO, n = 11 for hM3Dq CNO, P = 0.001 for social ability, P = 0.704 for social novelty, unpaired Holm-Sidak multiple t-test). **(E-F)** Increased interaction time ratio **(E)** and total social time **(F)** in hM3Dq group after acute activation of ChCs (n = 10 for EGFP CNO, n = 11 for hM3Dq CNO. In **(E)**, P = 0.002, in **(F)**, P = 0.003, unpaired t-test) **(G-J)** No difference between CTRL and hM3Dq group in social approach or social novelty test in the hM3Dq group after chronic activation of ChCs (n = 10 for EGFP CNO and 12 for hM3Dq CNO. In **(H)**, P = 0.885 for social ability, P = 0.904 for

social novelty, unpaired Holm-Sidak multiple *t*-test. In **(I)**, $P = 0.571$, unpaired *t*-test. In **(J)**, $P = 0.915$, unpaired *t*-test). Data are represented as mean ± SEM. ns $P>0.05$, $^{**}P < 0.01$.

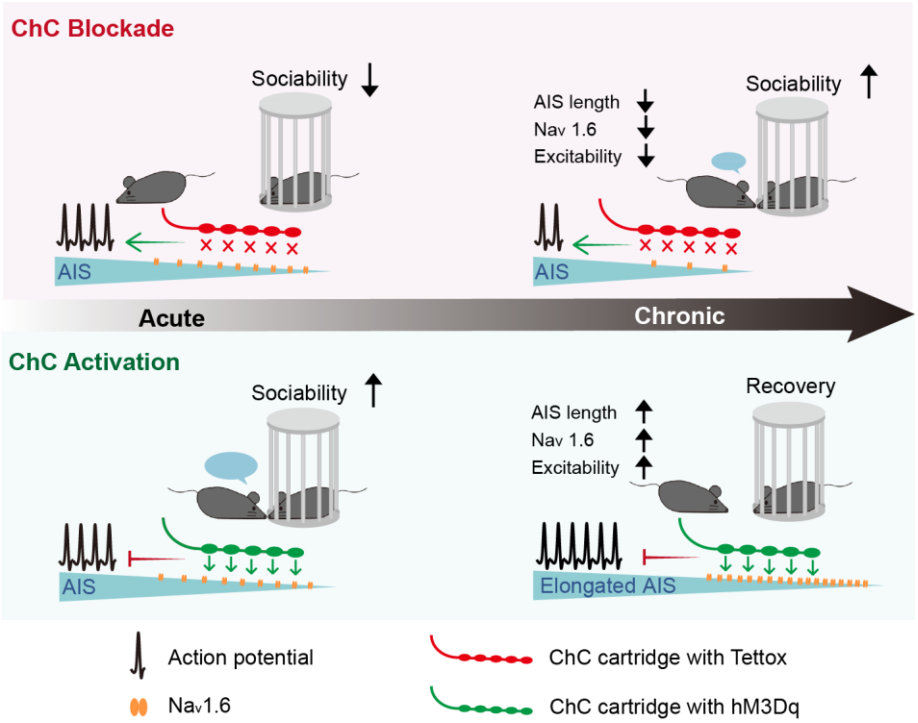

Fig. 8. Schematics illustrating sociability changes induced by alterations of ChC synaptic input are recovered when homeostatic plasticity of the AIS occurs.